



## D4.2

### Design of signalling schemes, protocols, and algorithms for energy-neutral devices

<b>Project number:</b>	101013425
<b>Project acronym:</b>	<b>REINDEER</b>
<b>Project title:</b>	REsilient INteractive applications through hyper Diversity in Energy Efficient RadioWeaves technology
<b>Project Start Date:</b>	1 <sup>st</sup> January, 2021
<b>Duration:</b>	42 months
<b>Programme:</b>	H2020-ICT-52-2020
<b>Deliverable Type:</b>	Report
<b>Reference Number:</b>	ICT-52-2020 / D4.2 / 1.00
<b>Workpackage:</b>	WP 4
<b>Due Date:</b>	30 <sup>th</sup> March, 2023
<b>Actual Submission Date:</b>	6 <sup>th</sup> April, 2023
<b>Responsible Organisation:</b>	TU GRAZ
<b>Editor:</b>	Benjamin J. B. Deutschmann
<b>Dissemination Level:</b>	PU
<b>Revision:</b>	1.00
<b>Abstract:</b>	Design of signaling schemes, protocols, and algorithms for energy-neutral devices. Report on the system design studies for achieving wireless power transfer, and efficient communications with energy neutral devices, while leveraging environment awareness.
<b>Keywords:</b>	RF, WPT, array near field, energy neutral devices, algorithms



The REINDEER project has received funding from the European Union's Horizon 2020 research and innovation programme under grant agreement No 101013425.

## **Editor**

Benjamin J. B. Deutschmann (TU GRAZ)

## **Contributors (ordered according to beneficiary numbers)**

Chesney Buyle, Bert Cox, Jarne Van Mulders, Gilles Callebaut (KU Leuven)

Ahmet Kaplan, Erik G. Larsson (LIU)

Benjamin J. B. Deutschmann, Thomas Wilding, Klaus Witrissal (TU GRAZ)

Ulrich Mühlmann (NXP)

## **Internal reviewers**

Liesbet Van der Perre (KU Leuven), Fredrik Tufvesson (ULUND)

## **Disclaimer**

*The information in this document is provided as is, and no guarantee or warranty is given that the information is fit for any particular purpose. The content of this document reflects only the author's view – the European Commission is not responsible for any use that may be made of the information it contains. The users use the information at their sole risk and liability.*

## Executive Summary

This deliverable reports on studies of signal processing and hardware design aspects that facilitate the achievable gains of a RadioWeaves infrastructure in the context of wireless power transfer (WPT). We investigate the benefits and challenges of exploiting *spatial diversity* to achieve efficient WPT and robust communication. Further, we address efficiency gains possibly achievable through *frequency diversity*, by exploiting high-peak-to-average power ratio (PAPR) waveforms. Based on measurements and real hardware implementations, our findings confirm the potential of environment-aware beamforming and the unprecedented WPT efficiency gains of a RadioWeaves infrastructure envisioned by the REINDEER consortium.

While a RadioWeaves infrastructure bears great potential for WPT, and particularly w.r.t. the interaction with energy neutral (EN) devices, there are challenges to be overcome to make use of this potential and leverage the available gains. We demonstrate how the environment awareness of RadioWeaves can aid in geometry-based beamforming to solve the initial access problem. We verify that physically large, or distributed radio infrastructures operating at sub-10 GHz achieve the gains predicted in the REINDEER deliverable D4.1 [1]. By means of synthetic aperture measurements, we show that a RadioWeaves infrastructure can lift the receivable power at the device side from the microwatt to the milliwatt range while transmitting over distances greater than 10 m. The apertures being physically large or distributed aid in regulatory-compliant beamforming and these outstanding efficiencies, as envisioned in [1]. We highlight the value of both measured channel state information (CSI), and CSI predicted based on a geometric channel model, which hints at the synergies of positioning and environment awareness with geometry-based beamforming to establish robust and energy-efficient radio links. We compare both types of CSI and show a first method of combining their information in a closed-loop approach. As a byproduct of our analysis, we find the fundamental performance limits of a reciprocity-based beamformer subject to imperfect CSI and the limits of random beamforming, also known as opportunistic beamforming. We compare a range of geometry-based beamformers with a reciprocity-based beamformer. For a bistatic backscatter communication setup, we further introduce a beamforming scheme for direct-link interference suppression. Decreasing the necessary dynamic range of the infrastructure and increasing the detection performance of EN devices, we implicitly address the energy efficiency ambitions of RadioWeaves.

Waveform design and exploiting frequency diversity have recently attracted significant research interest. Factoring in losses incurring due to broadband matching and increased hardware complexity, we demonstrate that efficiency gains are not always achievable. To evaluate how the end-to-end efficiency of a WPT system unfolds in a real implementation, the REINDEER consortium goes a step further and presents a prototype of an energy harvesting (EH) device. Evaluations on this new hardware platform will be addressed in the REINDEER deliverable D4.3 [2], together with algorithms leveraging synergies of environment-aware infrastructures with more efficiency. D4.3 marks the final deliverable of WP4 and will show concluding results of the consortium w.r.t. providing WPT as a service of a RadioWeaves infrastructure.

# Contents

<b>1</b>	<b>Introduction</b>	<b>1</b>
<b>2</b>	<b>Signal processing for beamforming, channel estimation and positioning</b>	<b>3</b>
2.1	Geometry-based channel prediction for WPT . . . . .	4
2.1.1	Geometry-based beamformers . . . . .	5
2.1.2	Comparison of measured and predicted CSI . . . . .	7
2.1.3	Geometry-based initial access . . . . .	12
2.2	Closed-loop approach based on DOA . . . . .	13
2.2.1	Direction of arrival-based positioning in the near field . . . . .	14
<b>3</b>	<b>Signal processing for backscatter-based communication</b>	<b>19</b>
3.1	Bistatic backscatter communication . . . . .	19
3.2	Proposed Transmission Scheme . . . . .	20
3.2.1	Phase 1: Channel Estimation at PanA . . . . .	21
3.2.2	Phase 2: Detection at PanB . . . . .	22
3.3	Proposed Interference Suppression Algorithm . . . . .	23
3.3.1	Channel Estimation at PanA . . . . .	23
3.3.2	Interference Suppression Algorithm . . . . .	23
3.4	Detection of the EN device . . . . .	24
3.5	Numerical Results . . . . .	26
<b>4</b>	<b>Signaling / Optimal waveform design</b>	<b>30</b>
4.1	Supplying multi-sine signal to rectifier circuits . . . . .	31
4.2	Performance with a commercial harvester circuit . . . . .	33
<b>5</b>	<b>Optimal hardware design</b>	<b>34</b>
5.1	Introduction . . . . .	34
5.2	Optimal transceiver design . . . . .	34
5.3	Joint-optimal circuit and antenna design . . . . .	36
<b>6</b>	<b>Summary</b>	<b>39</b>
<b>A</b>	<b>MISO channel model</b>	<b>41</b>
<b>B</b>	<b>Reciprocity Property of Radio Channels</b>	<b>43</b>
<b>C</b>	<b>Confidence associated with uncertainty intervals</b>	<b>44</b>
	<b>Bibliography</b>	<b>48</b>

# List of Acronyms

- 2D** two-dimensional. 14
- 3D** three-dimensional. 13
- AC** alternating current. 31
- ADC** analog-to-digital converter. 1
- AOA** angle-of-arrival. 17
- BC** backscatter communication. 19
- BD** backscatter device. 19
- CA** carrier emitter. 19
- CSI** channel state information. II, 1
- CSP** contact service point. 3
- CW** continuous wave. 31
- DC** direct current. 30, 31
- DLI** direct link interference. 19
- DM** diffuse multipath. 6
- DOA** direction-of-arrival. 13
- EH** energy harvesting. II, 2
- EN** energy neutral. II, 1
- END** energy neutral device. 13
- EVD** eigenvalue decomposition. 16
- FSS** frequency selective surface. 36
- i.i.d.** independent and identically distributed. 22
- IC** integrated circuit. 35
- IoT** Internet of Things. 1

**LoS** line-of-sight. 6

**MC** Monte Carlo. 10

**MIMO** multiple-input multiple-output. 3

**MISO** multiple-input single-output. 4

**MMSE** minimum mean square error. 3

**MRT** maximum ratio transmission. 3

**MUSIC** MUltiple SIgnal Classification. 16

**NP** Neyman-Pearson. 19

**P1** Phase 1. 20

**P2** Phase 2. 20

**PanA** Panel A. 20

**PanB** Panel B. 20

**PAPR** peak-to-average power ratio. II, 30

**PDF** probability density function. 11

**PW** planar wavefront. 5

**RCS** radar cross section. 16

**RF** radio frequency. 4

**RW** RadioWeave. 4

**SIMO** single-input multiple-output. 43

**SINR** signal-to-interference-plus-noise ratio. 20

**SISO** single-input single-output. 11

**SMC** specular multipath component. 5

**SNR** signal-to-noise ratio. 7

**S-parameter** scattering parameter. 4

**SW** spherical wavefront. 5

**UWB** ultrawideband. 7

**VNA** vector network analyzer. 4

**WPT** wireless power transfer. II, 1

**XETS** cross exponentially tapered slot. 7

**ZF** zero-forcing. 3

# List of Figures

2.1	Synthetic aperture measurement scenario. . . . .	8
2.2	Comparison and fundamental limits of reciprocity-based beamformers. . . . .	10
2.3	Beamformers applied at $p_{EN}^{(1)}$ , $PG$ distribution evaluated around $p_{EN}^{(1)}$ . . . . .	11
2.4	Beamformers applied at $p_{EN}^{(2)}$ , $PG$ distribution evaluated around $p_{EN}^{(2)}$ . . . . .	12
2.5	Beamformers applied at $p_{EN}^{(1)}$ , $PG$ distribution evaluated around $p_{EN}^{(2)}$ . . . . .	12
2.6	Beam sweep of a planar wavefront beamformer. . . . .	13
2.7	Graphical overview of the closed loop approach in 2D. . . . .	14
2.8	Simulated power gain for two EN devices. . . . .	16
2.9	Simulated 2D spatial spectrum in the Techtile environment. . . . .	17
2.10	3D DoA estimation plots in the Techtile environment. . . . .	17
3.1	The system model of the multi-antenna bistatic backscatter communication. . . . .	21
3.2	The transmission scheme of the bistatic setup. . . . .	21
3.3	The detection performance of EN device at PanB. . . . .	28
3.4	The ratio of the backscatter plus direct link power to the backscatter link power. . . . .	28
4.1	Single diode rectifier circuit in PySpice simulations. . . . .	31
4.2	One stage voltage doubler rectifier circuit in PySpice simulations. . . . .	31
4.3	Comparison of efficiency for single and multi-sine signals for multiple input powers. . . . .	32
5.1	Block diagram of the harvesting demonstrator to evaluate different use-cases. . . . .	35
5.2	Optimal antenna design, 915 MHz and 2.45 GHz . . . . .	37
5.3	Optimal antennas (manufactured), 915 MHz and 2.45 GHz. . . . .	38
C.1	Evaluation of confidences within $n\sigma$ -intervals versus channel SNR. . . . .	45

# List of Tables

2.1	List of Measurement Parameters . . . . .	9
2.2	SMC Power Budgets and Optimized Parameters . . . . .	9
3.1	Mathematical Notations . . . . .	22
3.2	Simulation Parameters . . . . .	27
4.1	RF-to-DC conversion efficiency measurement with the e-peas AEM40940 harvester	33
5.1	Specifications of the Demonstrator Hardware . . . . .	36

# Chapter 1

## Introduction

A RadioWeaves infrastructure leverages geometric environment information to provide services, such as ultra-reliable communication, positioning, and wireless power transfer (WPT). Paired with the operation of (batteryless) energy neutral (EN) devices, it enables massive yet sustainable deployments of connected devices for the Internet of Things (IoT). Outstanding efficiencies are achieved by coherently focusing radio waves from many distributed antennas to the position of an EN device. We demonstrate that the achievable gains of physically large apertures operating at sub-10GHz can lift the receivable power at the device side from the microwatt to the milliwatt range while transmitting over distances greater than 10 meters. Beamforming methods accomplishing this task commonly rely on *measured* channel state information (CSI), which is not available for the initial access to the device. We found that geometric models of wireless propagation channels allow to predict CSI and beamform power to spatial locations solely based on geometric information. Combined with its capability of positioning EN devices, geometric information aids a RadioWeaves infrastructure in leveraging unprecedented array gains, ultimately turning massive, sustainable, and cost-effective IoT deployments into reality.

This document reports on studies regarding many signal processing aspects that facilitate the achievable gains of a RadioWeaves infrastructure: In Section 2.1, we analyze geometry-based beamformers that predict CSI based on geometric environment information. We evaluate their performances on synthetic array measurements and compare them against a measurement-based beamformer subject to noisy CSI.

Section 2.2 shows an exemplary implementation of a closed-loop approach, which unites the two types of CSI: It uses measured CSI (i.e., channels estimated from a received pilot sequence) to infer the position of an EN device on the uplink. It subsequently predicts CSI using a geometry-based channel model based on the inferred position of the EN device.

The REINDEER consortium envisions massive deployments of batteryless EN devices that operate energy-efficiently using backscatter communication. Backscattered signals from EN devices have a very low amplitude compared with the carrier signal (i.e., the direct link interference between two RadioWeaves) they are modulating. This in turn necessitates high-resolution analog-to-digital converters (ADCs) that provide the necessary dynamic range to detect these backscattered signals buried in a dominant carrier. In Chapter 3, we present a novel algorithm that computes beamforming weights that project the direct link signal into the nullspace of the receiver and thereby decreases the necessary dynamic range (and power consumption of the infrastructure) and increases the detection performance of EN devices.

Diversity is what enables most of the promising features of a RadioWeaves infrastructure. While

beamforming exploits *spatial diversity* to achieve high constructive interference, i.e., array gains, or destructive interference, i.e., cancellation, through beamforming, recent literature indicates that *frequency diversity* may be exploited to overcome and even benefit from the nonlinear behavior of the frontends of EN devices. In Chapter 4, we investigate the achievable efficiency gains at the frontend in the context of RadioWeaves. This is done by means of both simulation of a simplified circuit and measurement of a state-of-the-art energy harvesting (EH) chip.

As a final step, after analyzing the performance of a state-of-the-art EH chip, we design a demonstrator of an EH device in Chapter 5 and discuss the challenges that come along: An optimal transceiver system design that minimizes parasitic losses, exhibits broad matching, behaves more robustly against detuning, and finds the optimal trade-off between power consumption and data rate. We demonstrate a method of directly matching the EH circuit to the antenna and thereby omitting a lossy matching network, which results both in an efficient design and a small form factor.

*Relations to other REIDNEER deliverables:* This deliverables presents measurement-based validation of concepts and potential forecasted in the REINDEER deliverables D2.1 [3] and D4.1 [1]. The measurements conducted also constitute a validation of some channel modeling aspects discussed in D2.1 [3]. Aspects regarding positioning, and exploiting position-related information as well as synchronization will be found in D3.3 [4]. Particularly the analysis of the reciprocity-based beamformer subject to noisy CSI estimates in Section 2.1.2 is strongly related to a system suffering from imperfect phase synchronization, as discussed in D2.3 [5, Section 4.1.2].

## Chapter 2

# Signal processing for beamforming, channel estimation and positioning

We investigate signal processing techniques for beamforming in the application context of WPT. Particularly, we introduce beamforming concepts on the downlink by means of precoding weights for phased arrays. We do this while keeping in mind that the radio channels are reciprocal<sup>1</sup> and the precoding techniques also apply to the uplink.

There exist several downlink precoding schemes for multiple-input multiple-output (MIMO) systems like maximum ratio transmission (MRT), zero-forcing (ZF), or minimum mean square error (MMSE)<sup>2</sup> [3], [7]. Each of them is designed to achieve a specific goal (e.g., power-optimal transmission, inter-user interference mitigation, and receiver noise suppression). They all have in common that they require CSI to compute precoding weights  $w$ . Applying a precoding method will result in beamforming, i.e., the coherent summation of transmitted waves (on the downlink) in a beam or focal point, depending on the extent of the apertures and operating distances involved. Precoding using *measured* CSI based on uplink pilots will result in *reciprocity-based*<sup>3</sup> beamforming. That is, precoding weights  $w$  for the downlink are computed from a channel estimate  $\hat{h}$ , estimated from a received pilot sequence in the uplink, and inherently exploiting the *reciprocity property* of radio channels (see Appendix B).

We show how geometric environment information can be leveraged to *predict* CSI (without having measured CSI available) and thus performing geometry-based beamforming. This is of particular interest for the initial access to EN devices, before an EN device is able to transmit a pilot sequence and thus measurement-based channel state estimation is not possible. The quality of predicted CSI depends on the accuracy of the modeled channels, where imperfect CSI manifests in power losses. We evaluate how well our geometry-based channel model derived in [8] is capable of predicting CSI for WPT.

As a byproduct of our analysis, we find the fundamental limits of *random beamforming*, sometimes also termed *opportunistic beamforming* [9], a method applicable when no CSI is available (as demonstrated in [10]) or lacks some crucial CSI like phase information (as demonstrated in [5]).

---

<sup>1</sup>In our analysis we consider radio channels between the antennas of a contact service point (CSP) and an EN device. Possibly non-reciprocal parts of their frontends are not considered in this analysis.

<sup>2</sup>Sometimes also referred to as “regularized” ZF [6].

<sup>3</sup>Although geometry-based beamforming likewise exploits the reciprocity-property of radio channels, the term *reciprocity-based* will denote beamforming based on measured CSI for the remainder of this document.

The remainder of this chapter is structured as follows. In [10] we introduce geometry-based beamformers, which we summarize in Section 2.1.1. In Section 2.1.2 we compare these geometry-based beamformers with a measurement-based beamformer depending on the quality of measured CSI available. The evaluation is based on synthetic array measurements acquired with a vector network analyzer (VNA). Section 2.1.3 shows how the geometry-based beamformers perform at solving the initial access problem in a real-life scenario. Section 2.2 shows an exemplary implementation of a closed-loop approach, which unites the two types of CSI: It uses measured CSI (i.e., channels estimated from a received pilot sequence) to infer the position of an EN device on the uplink. It subsequently predicts CSI using a geometry-based channel model based on the inferred position of the EN device.

*Notations:* For the remainder of this deliverable, lowercase bold letters  $\mathbf{x}$  will be used to denote vectors, while uppercase bold letters  $\mathbf{X}$  denote matrices. Further,  $[\mathbf{x}]_i$  denotes the  $i^{\text{th}}$  element of vector  $\mathbf{x}$ , and  $[\mathbf{X}]_{i,j}$  denotes the element of row  $i$  and column  $j$  in matrix  $\mathbf{X}$ . We use  $\mathbf{x}^T$  and  $\mathbf{x}^H$  to denote the transpose and Hermitian transpose of  $\mathbf{x}$ , respectively. The  $p$ -norm of vector  $\mathbf{x}$  is denoted as  $\|\mathbf{x}\|_p$ , while we omit the subscript notation for the Euclidean norm, i.e.,  $\|\mathbf{x}\|$  given  $p = 2$ .

## 2.1 Geometry-based channel prediction for WPT

We model a multiple-input single-output (MISO) system, aiming to transmit power wirelessly from the RadioWeave (RW) infrastructure, to a single EN device. We assume a narrowband frequency-flat fading channel  $\mathbf{h} \in \mathbb{C}^{L \times 1}$  that models the transmission coefficients, i.e., scattering parameters (S-parameters), from each transmit antenna  $\ell \in \{1, \dots, L\}$  to the receiving antenna of the EN device. The RW transmits an overall power  $P_t$  distributed via the weights  $\mathbf{w} \in \mathbb{C}^{L \times 1}$  via its antennas, where  $\|\mathbf{w}\| = 1$ . The EN device receives a complex baseband amplitude, i.e., a phasor,

$$y = \mathbf{h}^T \mathbf{w} \sqrt{P_t} + n \quad (2.1)$$

where we assume that the power of the noise  $n$  (i.e., for ambient energy harvesting) is negligible when compared to intentional WPT. Consequently, the radio frequency (RF)-RF transmission efficiency is

$$\frac{P_r}{P_t} = \frac{|y|^2}{P_t} \approx |\mathbf{h}^T \mathbf{w}|^2 = PG \quad (2.2)$$

where  $P_r = |y|^2$  is the power received by the EN device and  $PG$  denotes the “effective” MISO path gain including the antenna gains, polarization gain, and array gain according to the definition in [1, eq. (2.4)].

A beamforming method aims to choose the optimum weights that maximize the path gain in (2.2). These power-optimal weights are well-known to be computed through MRT as

$$\mathbf{w} = \frac{\mathbf{h}^*}{\|\mathbf{h}\|} \quad (2.3)$$

which demands knowledge of the channel vector  $\mathbf{h}$ . For the initial access to an EN device, i.e., before the initial wake-up and reception of a backscattered signal, this CSI is unknown and the weights  $\mathbf{w}$  cannot be computed through (2.3).

The challenge of the initial access procedure is to deliver power to an EN device that exceeds its sensitivity limit  $P_{r,\min}$ , i.e., its minimum wake-up power, given that neither the channel vector  $\mathbf{h}$ , nor the device position  $\mathbf{p}$  are known. Having a calibrated<sup>4</sup> array with known antenna positions  $\mathbf{p}_{\text{RW}}^{(\ell)}$ , beamforming weights can be computed based on a geometry-based channel model  $\tilde{\mathbf{h}}(\mathbf{p})$ . To compensate for the a priori unknown EN device position  $\mathbf{p}$ , a common strategy is to perform an exhaustive search, also known as beam sweeping. After a successful wakeup of an EN device, it can transmit its first signal. CSI can be estimated at the RW and the channel estimate  $\hat{\mathbf{h}}$  can be used to conduct reciprocity-based MRT.

## 2.1.1 Geometry-based beamformers

We introduce geometry-based beamformers, which compute the beamforming weights  $\mathbf{w}_{\text{PW}}$  for a planar wavefront (PW), and  $\mathbf{w}_{\text{SW}}$  for a spherical wavefront (SW). Both work with the vectorial distances  $\mathbf{r}_\ell = \mathbf{p} - \mathbf{p}_{\text{RW}}^{(\ell)}$  from each transmit antenna  $\ell$  of the RW to an arbitrary point  $\mathbf{p}$  in space. When the position of an EN device  $\mathbf{p}_{\text{EN}}$  is known, these weights can be used to conduct beamforming without measured CSI available, i.e., by computing the weights per specular multipath component (SMC) from the known geometry. In the initial access procedure, however, both measured CSI and the positions of EN devices are unknown. Thus, the two-dimensional or three-dimensional parameter spaces of the respective beamformer have to be searched through beam sweeping.

In the following, we derive the beamforming weights  $\mathbf{w}$  through MRT on a modeled geometry-based channel  $\tilde{\mathbf{h}}$  using (2.3). Deviations from the “true” channel manifest as power losses, such that geometry-based beamformers based on more detailed channel models perform more efficiently. The same holds for a reciprocity-based beamformer, which has an efficiency that is dependent on the quality of the estimated CSI. We derive its expected efficiency, i.e., its path gain, as a function of the quality of CSI analytically in the appendix of [10] and we compare its performance with our geometry-based beamformers in Section 2.1.2.

### 2.1.1.1 Planar wavefront beamformer

The PW beamformer computes weights  $\mathbf{w}_{\text{PW}}$  that cause the RW to transmit planar wavefronts towards the targeted angular direction  $[\theta \ \varphi]^T$ , where  $\theta$  and  $\varphi$  are the look angles in local spherical coordinates of the RW pointing from its center of gravity  $\mathbf{p}_{\text{RW}}$  to the EN device position  $\mathbf{p}$ . The spherical coordinates translate to the wave vector defined as [11, p.43]

$$\mathbf{k} = \begin{bmatrix} k_x \\ k_y \\ k_z \end{bmatrix} = k_0 \begin{bmatrix} \sin \theta \cos \varphi \\ \sin \theta \sin \varphi \\ \cos \theta \end{bmatrix} \in \mathbb{R}^{3 \times 1}, \quad (2.4)$$

with  $k_0 = \frac{2\pi}{\lambda}$  denoting the spatial angular frequency. With the array layout captured in  $\mathbf{P}_{\text{RW}} = \begin{bmatrix} \mathbf{p}_{\text{RW}}^{(1)} & \dots & \mathbf{p}_{\text{RW}}^{(L)} \end{bmatrix} \in \mathbb{R}^{3 \times L}$ , the PW beamforming weights can be computed as

$$\mathbf{w}_{\text{PW}} = \frac{\tilde{\mathbf{h}}_{\text{PW}}^*}{\|\tilde{\mathbf{h}}_{\text{PW}}\|} \text{ with } \left[ \tilde{\mathbf{h}}_{\text{PW}} \right]_\ell = e^{j\mathbf{p}_{\text{RW}}^{(\ell)\top} \mathbf{k}}. \quad (2.5)$$

<sup>4</sup>We consider the linear error network before the antennas as characterized and compensated for, i.e., we can coherently control the phasors at the phase centers of the antennas.

### 2.1.1.2 Spherical wavefront LoS beamformer

A SW beamformer computes weights  $\mathbf{w}_{\text{SW}}$  that cause the RW to transmit spherical wavefronts towards the three-dimensional position  $\mathbf{p}$ . It projects the distances  $r_\ell$  onto wave vectors  $\mathbf{k}_\ell$  defined w.r.t. the phase center of each antenna  $\ell$ . Consequently, the SW line-of-sight (LoS) beamformer weights are given by

$$\mathbf{w}_{\text{SW}} = \frac{\tilde{\mathbf{h}}_{\text{SW}}^*}{\|\tilde{\mathbf{h}}_{\text{SW}}\|} \quad \text{with} \quad \left[ \tilde{\mathbf{h}}_{\text{SW}} \right]_\ell = e^{-j\mathbf{r}_\ell^T \mathbf{k}_\ell} = e^{-jk_\ell \|\mathbf{r}_\ell\|}, \quad (2.6)$$

essentially modeling the phase shifts due to the distances  $\|\mathbf{r}_\ell\|$  traveled from each antenna  $\ell$  to the EN device.

### 2.1.1.3 Spherical Wavefront SMC Beamformer

Our most sophisticated geometry-based beamformer is the SMC SW beamformer. It is based on the geometry-based channel model in Appendix A, which corresponds to the channel model introduced in the REINDEER deliverable D1.2 [8], but formulated for a MISO system and omitting diffuse multipath (DM) in this investigation. It takes gain patterns of the used antennas into account, as well as image sources up to the 1<sup>st</sup> order. Consequently, it computes beamforming weights from

$$\tilde{\mathbf{h}}_{\text{SMC}} = \sum_{k=1}^K \mathbf{h}_k(\mathbf{p}), \quad (2.7)$$

with  $\mathbf{h}_k(\mathbf{p})$  denoting the channel vectors for every SMC  $k \in \{1 \dots K\}$  from the model in (A.2). This establishes a simultaneous multibeam transmission, exploiting reflections from the walls and the floor. Therefore, it needs a geometric environment model to compute the  $K$  virtual mirror sources of the RW. Uncertainties in the environment model affect the locations of SMC beams and their phases at the intended focal point position  $\mathbf{p}$ . The impact of the latter may be quite severe, since unaligned phases of SMC beams may even interfere destructively at  $\mathbf{p}$ . Possibly unknown phase shifts incurring due to specular reflections may also cause this effect. During the initial access phase, we propose to use a scheme of varying SMC beam phases to compensate for these possibly unknown phases, either randomly as proposed in [12], or by iterating through a predefined codebook. The objective is to find optimal phase shifts  $\tilde{\varphi}_k$  for alternative weights

$$\tilde{\mathbf{w}}_{\text{SMC}} = \frac{\sum_{k=1}^K \mathbf{w}_k e^{j\tilde{\varphi}_k}}{\|\sum_{k=1}^K \mathbf{w}_k e^{j\tilde{\varphi}_k}\|} \quad \text{with} \quad \mathbf{w}_k = \frac{\mathbf{h}_k^*}{\|\mathbf{h}_k\|} \quad (2.8)$$

attempting to solve the optimization problem

$$\tilde{\boldsymbol{\varphi}} = \begin{bmatrix} \tilde{\varphi}_1 \\ \vdots \\ \tilde{\varphi}_K \end{bmatrix} = \arg \max_{\varphi_1 \dots \varphi_K} \left| \sum_{k=1}^K \mathbf{h}^T \mathbf{w}_k e^{j\varphi_k} \right|^2, \quad (2.9)$$

which optimizes the path gain and thus the received power at the EN device. Due to the fact that the “true” channel  $\mathbf{h}$  is generally unknown and measured CSI  $\hat{\mathbf{h}}$  is unavailable in the initial access phase, (2.9) can only be solved approximately, e.g., by random search or possibly through a grid search. After the initial wake-up of the EN device, feedback about the received power  $P_r$  may

become available and (2.9) can be solved efficiently. Note that the number of beam phases to be optimized is  $K - 1$ , i.e., the phase of one beam (e.g., the LoS beam, s.t.  $\tilde{\varphi}_1 = 0$ ) can be kept constant and all other beam phases are optimized.

Furthermore, a geometric environment model may not provide information on the reflection coefficients of surfaces dependent on their electromagnetic properties. A similar optimization approach can be followed to compensate for possibly unknown reflection coefficients  $\gamma_k$ . The objective is to find optimal reflection coefficients  $\tilde{\gamma}_k$  that optimize

$$\tilde{\gamma} = \begin{bmatrix} \tilde{\gamma}_1 \\ \vdots \\ \tilde{\gamma}_K \end{bmatrix} = \arg \max_{\gamma_2 \dots \gamma_K} \left| \frac{\sum_{k=1}^K \mathbf{h}_k^H(\gamma_k)}{\|\sum_{k=1}^K \mathbf{h}_k^H(\gamma_k)\|} \mathbf{h} \right|^2, \quad (2.10)$$

where the optimal phase shifts  $e^{j\tilde{\varphi}_k}$  in (2.8) can be applied to the vectors  $\mathbf{h}_k^H$  before computing (2.10). Although less crucial than the optimization of SMC beam phases, this optimization allows the beamformer to vary the power directed into each beam and thus pronounce strong links and attenuate weak links.

#### 2.1.1.4 Reciprocity-based beamformer

Only after an EN device has been woken up successfully for the first time, CSI can be obtained from a backscattered signal. We assume to acquire a noisy channel estimate

$$\hat{\mathbf{h}} = \mathbf{h} + \mathbf{n}_h \quad (2.11)$$

with the i.i.d. circular Gaussian noise samples  $[\mathbf{n}_h]_\ell \sim \mathcal{CN}(0, \sigma_h^2)$ . The efficiency of a reciprocity-based beamformer depends on the quality of the acquired CSI [13]. To express the quality of our channel estimate  $\hat{\mathbf{h}}$ , we define the channel signal-to-noise ratio (SNR) as

$$\text{SNR} = \frac{P_{\text{ch}}}{P_n}, \quad \text{where} \quad (2.12)$$

$$P_{\text{ch}} = \frac{1}{L} \|\mathbf{h}\|^2 \approx PG_{\text{SISO}} \quad (2.13)$$

is the channel power (which is actually an efficiency) and  $P_n = \sigma_h^2$  is the channel noise variance. The efficiency of the reciprocity-based beamformer versus channel SNR is derived in the appendix of [10] and performance assessments of all introduced beamformers are conducted in the following section.

### 2.1.2 Comparison of measured and predicted CSI

We use a synthetic array measurement testbed described in [8] to acquire channel vectors in a real-life scenario and subsequently evaluate the performance of the beamformers introduced in Section 2.1.1 on the measured data. A Rohde & Schwarz ZVA24 VNA is used in a two-port configuration to measure the transmission coefficient  $S_{21,\ell} \triangleq [\mathbf{h}]_\ell$  between a transmit antenna  $\ell$  connected to Port1 and a receiving antenna connected to Port2. The transmit antenna is attached to a large mechanical positioner which forms a synthetic array, i.e., we consecutively measure the channel entries  $[\mathbf{h}]_\ell$  at desired positions  $\mathbf{p}_{\text{RW}}^{(\ell)}$  parallel to the  $yz$ -plane (cf., the direct path in Fig. 2.1). We employ two cross exponentially tapered slot (XETS) antennas [14] which are ultrawideband (UWB) antennas but we only evaluate channels at a frequency  $f = 3.8$  GHz in this

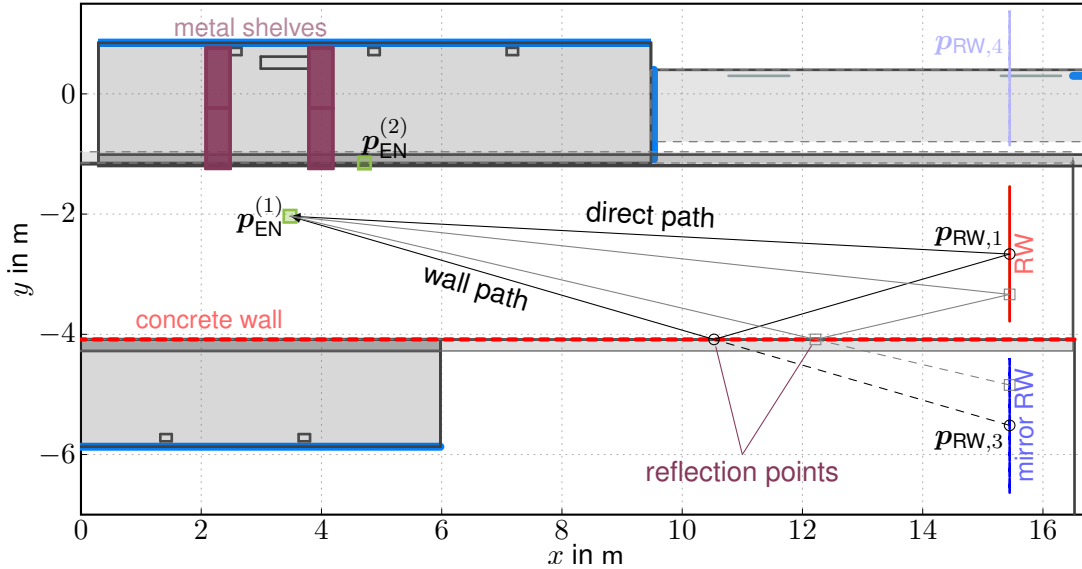


Figure 2.1: The measurement scenario: A long hallway with concrete walls. A large RW is indicated on the right side (positive  $x$ -direction) along with its virtual mirror sources centered around positions  $p_{RW,1}$ . The two measurement positions  $p_{EN}^{(1)}$  and  $p_{EN}^{(2)}$  of hypothetical EN devices are indicated on the left side.

study. The antennas were characterized in an anechoic chamber, such that we have knowledge of their gain patterns  $G(\theta, \varphi)$ . The measurement scenario<sup>5</sup> depicted in Fig. 2.1 is a long hallway where the synthetic RW is mounted on a bridge between two concrete walls. Measurement and scenario specific parameters are summarized in Table 2.1. The RW has a total of  $L_y \times L_z = 40 \times 25$  antennas and forms a physical aperture of  $l_y \times l_z = (2.24 \times 1.38) \text{ m}^2$ . We choose the two sidewalls and the floor as representative SMCs and use the corresponding  $K = 4$  mirror sources including the LoS for predicting channels with the SW SMC beamformer from Section 2.1.1.1. The process of mirroring of the RW across walls is described in the appendix of [10]. The receiving antenna is moved by another mechanical positioner in a  $\frac{3}{8}\lambda$ -spaced grid within the  $xy$ -plane to capture the spatial distribution of power around one antenna position chosen as hypothetical EN device. The measurements are conducted at two positions  $p_{EN}^{(1)}$  and  $p_{EN}^{(2)}$  in the hallway, where the latter is less favorable for beamforming but more relevant from a practical perspective due a metal shelf behind it, which is filled with water bottles and has a reflective metal grid mounted on its backside facing the negative  $x$ -direction. The measurement positions are located at distances  $\|r^{(1)}\| \approx 12.3 \text{ m}$  and  $\|r^{(2)}\| \approx 11.1 \text{ m}$  from the center of gravity of the RW.

We assume that our measured channels  $[h]_\ell$  are the “true”<sup>6</sup> channels given that we have a reasonably high measurement SNR. We compute separate weights  $w_k$  as defined in (2.8) to analyze the path gain  $PG_k$  for each of the  $K$  SMC beams. We apply these weights on the measured channel vector  $h$  and compute the achievable path gain for every SMC beam through MRT. The individual power budgets  $PG_k = |h^\top w_k|^2$  for each of these beams at measurement position  $p_{EN}^{(1)}$  are indicated in Table 2.2. The SMC  $k = 2$  corresponds to the image source from the floor,  $k = 3$  to the reflection in the negative  $y$ -direction and  $k = 4$  to the reflection in positive  $y$ -direction. With  $PG_1 \approx -33.4 \text{ dB}$ , the LoS is the strongest of the analyzed components and closely followed by  $PG_3 \approx -36.6 \text{ dB}$  which is a quite strong component, given that it suffers reflection losses at the

<sup>5</sup>A more comprehensive documentation of the measurement scenario and the measurement testbed can be found in [8].

<sup>6</sup>We make this assumption knowing that the “true” value of a measurand is generally unknown and our corrected measurement result is merely its best estimate [15].

Table 2.1: List of Measurement Parameters

Variable	Symbol	Unit	Value
Carrier frequency	$f$	GHz	3.8
RW (width $\times$ height)	$l_y \times l_z$	m <sup>2</sup>	$2.24 \times 1.38$
RW position	$\mathbf{p}_{\text{RW}}$	m	$[15.4, -2.6, 3.6]^T$
EN device position 1	$\mathbf{p}_{\text{EN}}^{(1)}$	m	$[3.5, -2, 1]^T$
EN device position 2	$\mathbf{p}_{\text{EN}}^{(2)}$	m	$[4.7, -1.1, 1.1]^T$
No. of TX antennas	$L_y \times L_z$	-	$40 \times 25$
RW antenna spacing	$\Delta_y, \Delta_z$	cm	5.7
No. of RX samples	$L_x^{\text{EN}} \times L_y^{\text{EN}}$	-	$8 \times 8$
RX sample spacing	$\Delta_x^{\text{EN}}, \Delta_y^{\text{EN}}$	m	$\frac{3}{8}\lambda$

Table 2.2: SMC Power Budgets and Optimized Parameters

Variable	Symbol	Unit	Values			
No. SMC	$k$	-	1	2	3	4
Path gain	$PG_k$	dB	-33.4	-52.7	-36.6	-49.0
Refl. coeff.	$\tilde{\gamma}_k$	dB	0	-43.32	-2.28	-4.8
Phase shift	$\tilde{\varphi}_k$	°	0	118	182	212

wall, longer distances to the EN device, and lower antenna gains. Component  $k = 4$  is comparably weak, because of the limited visibility of the wall: only 141 out of the  $L = 1000$  RW antennas of SMC 4 are visible from the EN device due to the limited extent of the respective wall, while all  $L$  antennas of SMC  $k = 3$  are visible. Furthermore, the optimization problems in (2.9) and (2.10) have been solved numerically to compute the optimum phase shifts  $\tilde{\varphi}_k$  and reflection coefficients  $\tilde{\gamma}_k$ . After the optimization, we get a modeled reflection coefficient of  $\tilde{\gamma}_3 = -2.28$  dB.

Due to the fact that the power-optimal weights are found by computing them through the assumed “true” channel  $\mathbf{h}$ , this optimized value would correspond closely to the “true” reflection coefficients of the walls, if the other channel parameters were known sufficiently well. The optimized reflection coefficient  $\tilde{\gamma}_4 = -4.8$  dB may therefore be a result of mismodeling, since we neglect diffraction effects in our visibility model and most of the visible part of the respective image source is located at the edge of the wall it is mirrored across.

From Table 2.2 it is evident that component  $k = 2$  is particularly weak, i.e.,  $PG_2$  is small compared to the other beams. Reflection coefficients of reflections at specular surfaces depend on the incidence angle of the waves and the electromagnetic parameters of the materials they are made of, particularly the relative permittivity of the concrete walls in our scenario. It is worth noting that the transmit and receive antennas of our synthetic array measurement testbed have polarization vectors  $\boldsymbol{\rho}$  aligned in parallel with the  $z$ -axis which are thus parallel to the normal vector of the floor. The reflection coefficient for such arrangements is described by [16, eq. (4-125)], which yields low values for typical relative permittivities of concrete (e.g.,  $\epsilon_r \approx 6$  [17]) and is generally unfavorable when compared to waves polarized orthogonal to the normal vector of specular surfaces. Polarization-dependent reflection coefficients, however, are not regarded in our channel model, thus the optimized value of  $\tilde{\gamma}_2$  corresponds to the unfavorable polarization plane of our antennas w.r.t. the floor.

We compare the beamformers introduced in Section 2.1.1 by means of their efficiencies, i.e.,

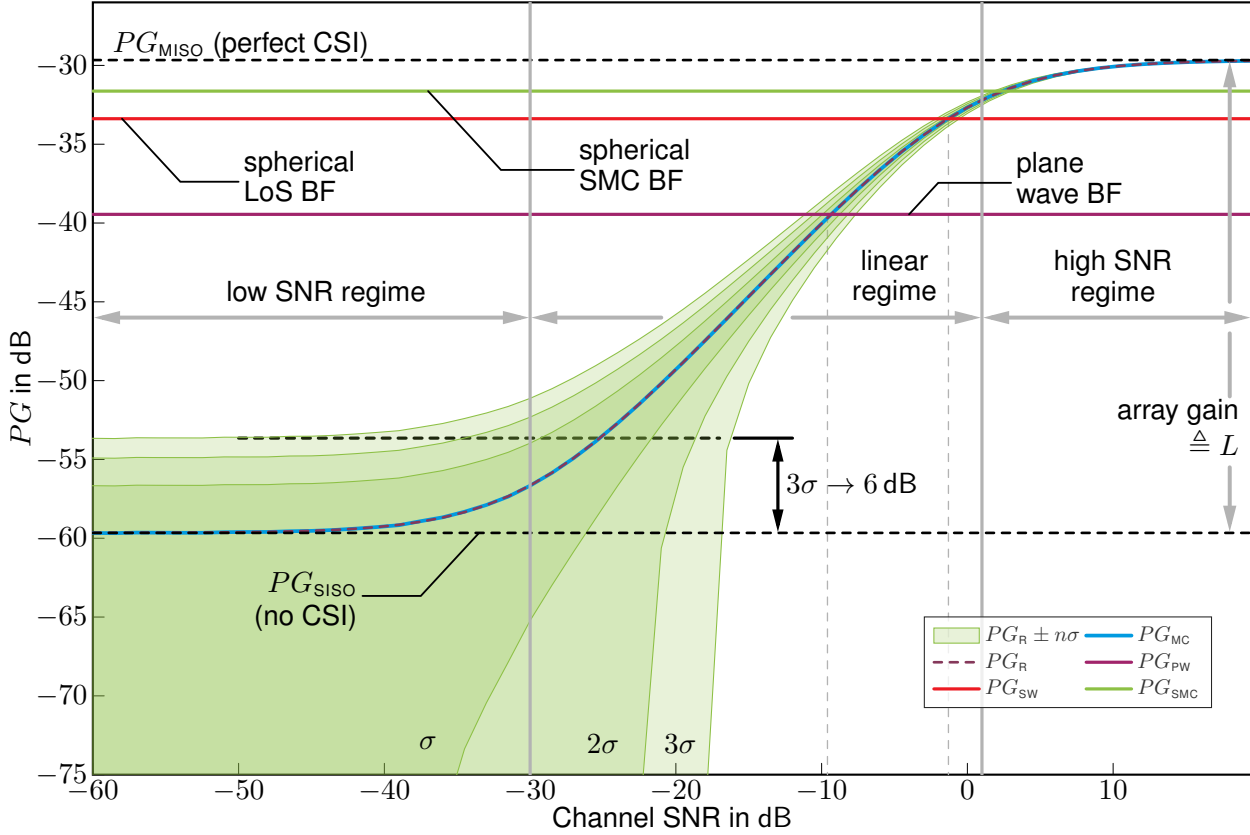


Figure 2.2: Comparison of the beamformers introduced in Section 2.1.1 when applied on a measured channel vector  $\mathbf{h}$  at  $\mathbf{p}_{\text{EN}}^{(1)}$ . The reciprocity-based beamformer is evaluated by means of an Monte Carlo analysis (i.e.,  $PG_{\text{MC}}$ ) and the analytical closed-form expression in (2.14) (i.e.,  $PG_{\text{R}}$ ) with the respective SNR regimes in (2.15).

evaluating their achieved  $PG$  in (2.2) with geometry-based channel vectors  $\tilde{\mathbf{h}}$  generated with the “true” EN device position  $\mathbf{p}_{\text{EN}}$ . We further investigate the efficiency of a reciprocity-based beamformer as a function of the quality of its CSI. Mishra and Larsson [13] have demonstrated that the  $PG$  reduces with imperfect CSI. Through our definition of the channel SNR in (2.12), we can find an approximate expression for the expected efficiency of a reciprocity-based beamformer

$$PG_{\text{R}} = \mathbb{E} \left\{ \left| \frac{\hat{\mathbf{h}}^H \mathbf{h}}{\|\hat{\mathbf{h}}\|} \right|^2 \right\} \approx \frac{\text{SNR}}{1 + \text{SNR}} (L P_{\text{ch}} + P_{\text{n}}) \quad (2.14)$$

$$\approx \begin{cases} P_{\text{ch}}, & \text{SNR} < 1/L \quad \dots \text{ low SNR regime} \\ L P_{\text{ch}} \text{ SNR}, & 1/L < \text{SNR} < 1 \quad \dots \text{ linear regime} \\ L P_{\text{ch}}, & \text{SNR} > 1 \quad \dots \text{ high SNR regime} \end{cases} \quad (2.15)$$

which is derived in the appendix of [10].

Fig. 2.2 shows the performance comparison of all introduced beamformers evaluated on the measured channel at  $\mathbf{p}_{\text{EN}}^{(1)}$ , which is assumed to be the “true” channel, i.e., perfect CSI. The analytical expression for the efficiency of the reciprocity-based beamformer in (2.14) is compared against a Monte Carlo (MC) analysis with  $M = 10^5$  realizations of (2.11), denoted  $PG_{\text{MC}}$ , where both curves show good correspondence. Furthermore, the standard deviation  $\sigma$  is evaluated both by means of the Monte Carlo (MC) analysis and the analytical result given in the appendix of [10] (valid for low SNRs). The indicated SNR regimes are defined in (2.15).

In the *low SNR regime*, the expected efficiency of the reciprocity-based beamformer is approximately equal to the path gain  $PG_{\text{SISO}}$  of an equivalent single-input single-output (SISO) system. However, through “random beamforming” corresponding to  $\hat{\mathbf{h}} = \mathbf{n}_h$ , an efficiency improvement of up to 6 dB is achievable within the  $3\sigma$ -interval in Fig. 2.2 (capturing approx. 98% of the path gain realizations<sup>7</sup>). The 6 dB gain results from  $\sigma \approx P_{\text{ch}} \approx PG_{\text{SISO}}$  in the low SNR regime (see the appendix of [10]), and thus  $PG_{\text{R}} + 3\sigma \approx 4PG_{\text{SISO}}$ , which is achievable irrespective of the number of antennas  $L$ . That is, even if using only e.g. 10% of the  $L = 1000$  transmit antennas, this 6 dB gain is still achievable, although the maximum achievable array gain (corresponding to the number of antennas used) reduces by 90%. This highlights that “random beamforming” beamforming gets increasingly inferior to e.g. geometry-based beamformers for massively increasing numbers of antennas (as will be shown below). The path gain will exceed this expected efficiency by more than 6 dB in less than 2% of the realizations, thus targeting higher gains will be practically unreasonable for most applications due to the large number of random weight realizations needed. The amplitude  $|y|$  is Rayleigh-distributed in this regime and the path gain is chi-squared distributed.

As the SNR increases,  $PG_{\text{R}}$  enters a regime of *linear* increase with the SNR, where both the amplitudes  $|y|$  and the path gain are normally distributed. Please refer to Appendix C where the confidence levels associated with the  $n\sigma$ -intervals are evaluated and the transition of distributions is illustrated. In this transition region from a “stochastic” beamformer to a deterministic beamformer, the relative uncertainty of the path gain decreases with increasing SNR.

Entering the high SNR regime,  $PG_{\text{R}}$  saturates at the MISO path gain  $PG_{\text{MISO}}$  requiring perfect CSI and leveraging the full array gain  $L$ .

We further compare the reciprocity-based beamformer to our geometry-based beamformers, defined in Section 2.1.1. The PW beamformer shows an efficiency loss of  $\Delta PG \approx 10$  dB, when compared with  $PG_{\text{MISO}}$  and is thus comparably inefficient, however, it can strongly reduce the duration of a possible beam sweeping procedure due to its reduced, two-dimensional search space. The SW LoS beamformer is approx. 6 dB more efficient than the PW beamformer and constitutes a good trade-off between model complexity and efficiency. In the given scenario, the SW SMC beamformer exhibits another 1.75 dB increase in efficiency, when compared with the SW LoS beamformer. It is based on our most complete SMC channel model and is dependent on multiple parameters as well as a geometric environment model. Given perfect CSI, a reciprocity-based beamformer could still attain 2 dB more efficiency than the SW SMC beamformer.

<sup>7</sup>In the low SNR regime, the path gain is a chi-squared distributed random variable with the intervals  $PG_{\text{R}} \pm n\sigma$  capturing {86.4, 95.0, 98.2}% of its probability density function (PDF) for  $n \in \{1, 2, 3\}$ . In the linear regime, it transitions to a Gaussian random variable where the intervals cover {68.3, 95.4, 99.7}%. These confidence levels are verified in Appendix C.

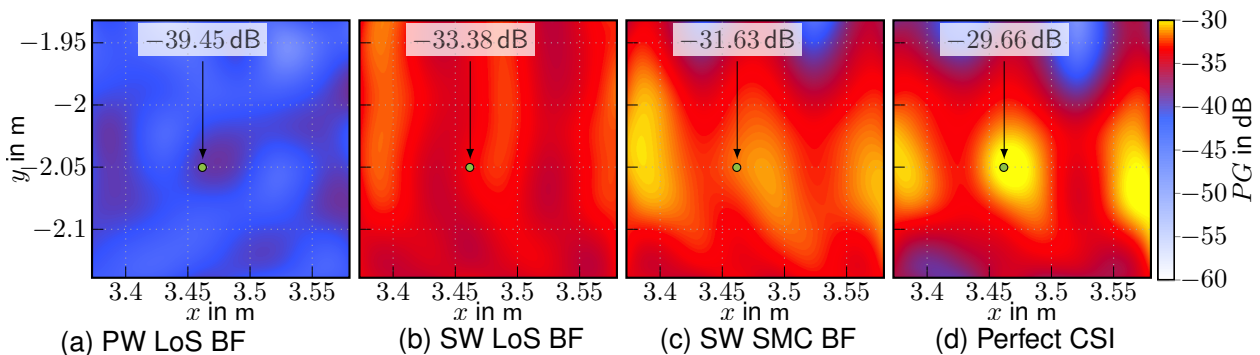


Figure 2.3: Beamformers applied at  $\mathbf{p}_{\text{EN}}^{(1)}$ ,  $PG$  distribution evaluated around  $\mathbf{p}_{\text{EN}}^{(1)}$ .

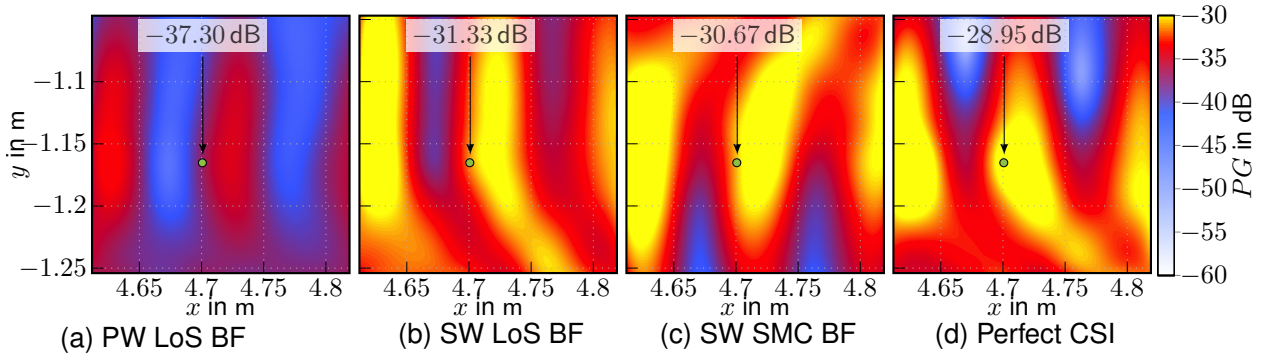


Figure 2.4: Beamformers applied at  $p_{\text{EN}}^{(2)}$ ,  $PG$  distribution evaluated around  $p_{\text{EN}}^{(2)}$ .

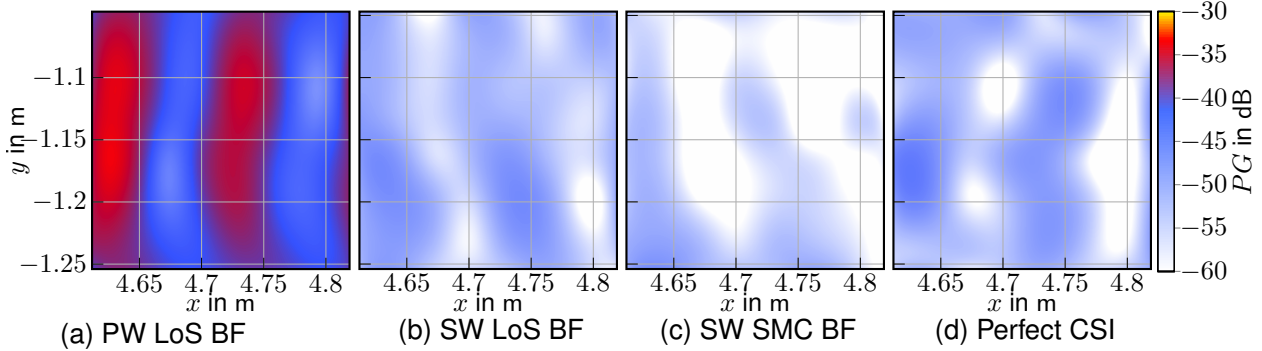


Figure 2.5: Beamformers applied at  $p_{\text{EN}}^{(1)}$ ,  $PG$  distribution evaluated around  $p_{\text{EN}}^{(2)}$ .

### 2.1.3 Geometry-based initial access

Fig. 2.3 and Fig. 2.4 are based on channel vectors measured across the  $8 \times 8$  grids of the EN device positions  $p_{\text{EN}}^{(1)}$  and  $p_{\text{EN}}^{(2)}$ . They show the interpolated path gain distributions at the grids when applying the described beamformers. For fairness, the PW beamformer is applied given the optimum angle of a beam sweep in the the range-azimuth plane (elaborated below in Fig. 2.6). It is observable that a rather homogeneous power distribution is achievable with the PW and SW beamformers around  $p_{\text{EN}}^{(1)}$  (see Fig. 2.3). Exploiting SMCs virtually increases the array aperture<sup>8</sup> and thus narrows its beam width (or width of its focal region, respectively), which is observable for the SW SMC beamformer and the reciprocity-based beamformer. The path gain distribution around  $p_{\text{EN}}^{(2)}$  (see Fig. 2.4) shows a strong standing wave pattern, originating from the bottles within the shelf and the metal grid mounted on its backside. Fig. 2.5 shows the path gain distribution around  $p_{\text{EN}}^{(2)}$  when beamforming to  $p_{\text{EN}}^{(1)}$ . It is clearly observable that the PW beamformer “pollutes” its environment with radiated power even in unintended positions. For the SW LoS and SMC beamformers, the power density around  $p_{\text{EN}}^{(2)}$  is strongly reduced since no specular components are exploited in its vicinity. However, the power density around  $p_{\text{EN}}^{(2)}$  increases again for the reciprocity-based beamformer that inherently exploits the complete channel *including diffuse reflections*.

In Fig. 2.6, we show the path gain of an exhaustive beam sweep with the PW beamformer, evaluated on a portion of the elevation-azimuth plane w.r.t the center of gravity of the RW. It achieves an efficiency of  $PG = -42.21$  dB at the “true” position of the EN device. In its vicinity across the azimuth plane, there is a fading pattern visible which originates from constructive and destructive interferences with the SMCs possibly caused by walls. As is indicated in the figure, the beam

<sup>8</sup>The array aperture increases virtually by not only using the LoS path but also the mirror sources depicted in Fig. 2.1.

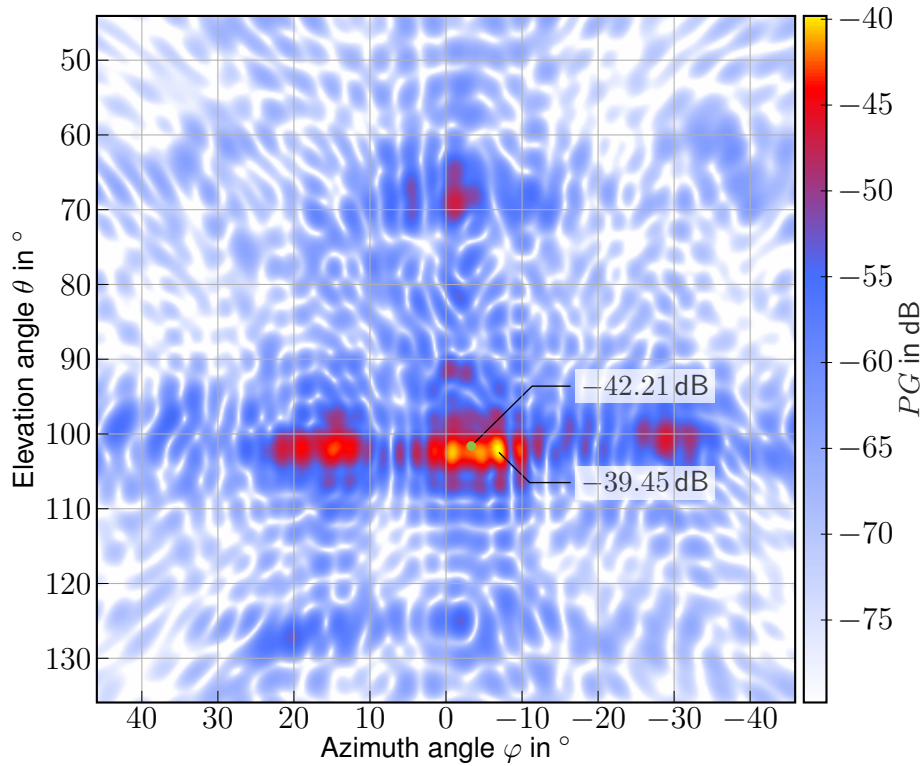


Figure 2.6: PW beamformer beamsweep at position  $p_{\text{EN}}^{(1)}$ : Depicted is the path gain evaluated on a portion of the elevation-azimuth plane. At the “true” position of the EN device, the PW beamformer achieves  $PG = -42.21$  dB, while it achieves a maximum of  $-39.45$  dB with constructive SMC interference.

sweep reaches its maximum path gain of  $-39.45$  dB not at the “true” position, but rather at an azimuth angle where constructive interference occurs. Therefore it is no coincidence that  $p_{\text{EN}}^{(1)}$  is located at a “peak” of the path gain distribution in Fig. 2.3 (a). The shape of that distribution is consequently a result of the interference of SMCs.

## 2.2 Closed-loop approach based on DOA

As mentioned in Section 3.2.1 of Deliverable D4.1 [1], the gain of physically large antenna arrays that focus power in the array near field is not only dependent on the direction angles, but on the range as well. The resulting focal point can charge EN devices faster or obtain a higher, low-power backscatter communication data rate than with conventional methods. Two methods can be applied to create such focal points. The first method uses the CSI coming from pilot signals sent out by the energy neutral device (END). This so-called “reciprocity-based” beamforming can be performed without knowing the actual position of the END. The second method uses the geometry of the setup, which includes the layout of the antenna arrays, the position of the END, and (possibly) a geometric model of the environment, in order to compute the channel vectors for beamforming. The latter has been investigated in Section 2.3 of D4.1 and validated in Section 2.1 of this deliverable. However, we have neither discussed how the position of the END can be estimated, nor, how the environment model is obtained.

This section will focus on the second power spot generation method. A closed-loop approach is given to acquire the three-dimensional (3D) END position from direction-of-arrival (DOA) estimates and to use the DOA information to compute the channel vectors for beamforming.

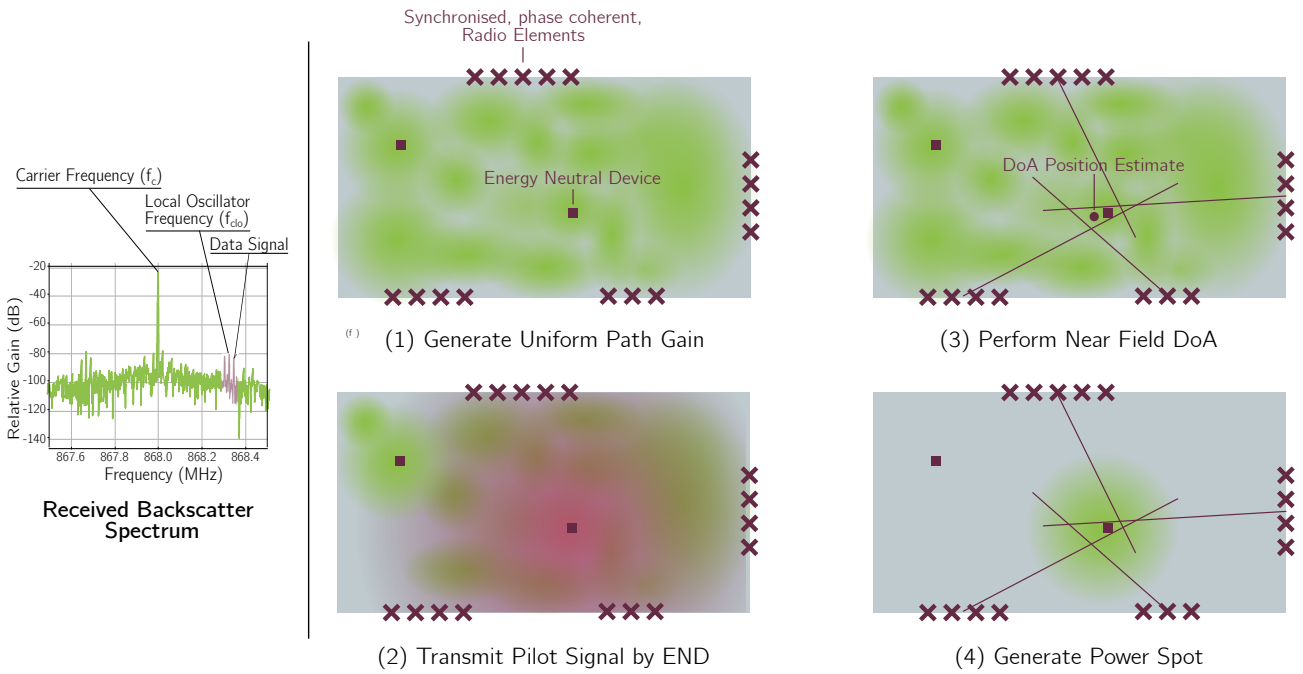


Figure 2.7: Graphical overview of the closed loop approach in 2D.

Knowing the actual position of the END has great potential from an application point-of-view. Real-time location data can improve safety, performance, experience and convenience in industrial, commercial and healthcare solutions.

### 2.2.1 Direction of arrival-based positioning in the near field

The researched closed-loop approach consists of four steps, where the last three can be repeated to increase the positioning accuracy and decrease the power spot size, and hence increase the power density at the EN position. A two-dimensional (2D) graphical illustration of this method can be found in Fig. 2.7. Four steps can be distinguished: (i) the creation of an (approximately) uniform power density through the entire room at a certain frequency (green), (ii) the transmission of a pilot signal by means of backscattering, (iii) performing DOA at the different radio elements and estimating the position of the END and (iv) the creation of a power spot at the estimated position. This four-step approach is tested inside the 3D channel model simulator described in [12]. In this simulator, the Techtile environment [18], [19] was reproduced with 280 transceiver antennas, grouped in four subarrays of  $(10 \times 10)$ ,  $(4 \times 13)$  and two  $(8 \times 8)$  antennas respectively, with half-wavelength spacing. An example of the three-dimensional model can be found in Figure 2.10. In what follows, two ENDS are added to the infrastructure: the first one close to the sidewalls at  $[1, 1, 1]^T$  and the second almost centrally at  $[4, 2, 1]^T$ .

#### 1. Generate a uniform power density and calculate the average charge time.

Just like the reciprocity beamforming method, the DOA based method is susceptible to the initial access problem. An initial energy budget is necessary at the END for sending out a pilot signal. This problem occurs at the start of the power spot generation or when a new node is introduced to the setup. Therefore, at certain periods in time, a quasi-uniform power density should be delivered throughout the whole room. In Section 4.1.2 of REINDEER deliverable D2.3 [5], the closed-form expression for the expected efficiency of a reciprocity-based beamformer, suffering

from synchronization losses is stated as

$$PG_R = \frac{\mathbb{E} \left\{ |\mathbf{h}^T \mathbf{s}|^2 \right\}}{P_{\text{tx}}} = \frac{1}{\|\mathbf{h}\|^2} \left( \|\mathbf{h}\|_4^4 + \underbrace{2 \binom{L}{2} P_{\text{ch}}^2 e^{-\sigma_\varphi^2}}_{\approx L^2} \right) \quad (2.16)$$

$$\approx \begin{cases} \frac{\|\mathbf{h}\|_4^4}{\|\mathbf{h}\|^2} & \text{Var}\{\varphi_\ell\} > \ln \|\mathbf{h}\|^4 - \ln \|\mathbf{h}\|_4^4 \\ L P_{\text{ch}} e^{-\sigma_\varphi^2}, & \ln 2 < \text{Var}\{\varphi_\ell\} < \ln \|\mathbf{h}\|^4 - \ln \|\mathbf{h}\|_4^4 \\ L P_{\text{ch}}, & \text{Var}\{\varphi_\ell\} < \ln 2 \end{cases} \quad (2.17)$$

By introducing a random phase error to each antenna element on purpose, the system is pushed into the low synchronization regime and thus noncoherent operation. With circularly-symmetric complex Gaussian phase errors, i.e.,  $\varphi_\ell \sim \mathcal{N}(0, \sigma_\varphi^2)$  with the weight vector elements  $[\mathbf{w}]_\ell = e^{j\varphi_\ell} [\mathbf{h}]_\ell^* / \|\mathbf{h}\|$ , “random beamforming” is performed and may achieve a  $PG$  improvement of up to 8.7 dB compared to SISO systems<sup>9</sup> when applied on the measured channel vector from Section 2.1.2. From Figure 4.1 in D2.3, the phase error standard deviation should be chosen above  $\sigma_\varphi \geq 160^\circ$ . Simulation results of this quasi-uniform path gain for the two aforementioned positions are calculated for a 2D plane at 1 m height and depicted in Fig. 2.8. The transmit power  $P_{\text{tx}}$  is set to 0 dB. The average simulated path gain is  $-41.9$  dB, and the achieved path gain at the center node is above this average ( $-38.6$  dB), yet below this average at the corner node ( $-42.6$  dB). For an END with an E-Peas AEM30940 energy harvesting chip with an efficiency of 48 % and an STM32L011F3 chip (an ARM Cortex-M0 based MCU) for frequency shifted backscattering with a power consumption of 200  $\mu\text{A}$  at 1.8 V, it would take respectively 17.2 s and 43.2 s to charge the proposed central and corner END when the transmitters have an output power of 15 dB.

## 2. Transmit pilot signals.

To eliminate the high power consumption of an active radio transmitter at the END, backscatter communication is chosen for sending out pilot signals. In Section 3.1, a more in-depth review on signal processing for backscatter-based communication is given. Backscattering in its most simple implementation switches the load of an antenna based on the digital pilot signal. In the closed-loop approach, this means an alteration of the omnipresent RF signals, generated by the random beamformer, resulting from the quasi-uniform field at a certain frequency. This carrier wave is either reflected or absorbed, resulting in a mixing process of this carrier signal and the information signal.

To eliminate the self-interference problem, frequency translation backscattering is applied by adding a local oscillator to the END, resulting in a data signal shifted away in the frequency domain from the carrier, as explained in D4.1 [1]. The added local oscillator contributes to a higher power consumption, yet it is an excellent compromise for the gained backscatter link SNR. In this scenario, the received power of the backscattered signal at the bistatic, dislocated receiver (from D4.1) is given by:

$$P_{\text{r,b}} = \sigma (1 - |\Gamma_t|^2) (1 - |\Gamma_r|^2) \left( \frac{\lambda}{4\pi d_1 d_2} \right)^2 \frac{P_t G_{t,1} G_r}{4\pi} |\boldsymbol{\rho}_t \cdot \boldsymbol{\rho}_b|^2 |\boldsymbol{\rho}_b \cdot \boldsymbol{\rho}_r|^2. \quad (2.18)$$

<sup>9</sup>In Section 2.1.2, we have shown that an improvement of up to 6 dB can be achieved within the  $3\sigma$ -interval covering 98 % of the weight realizations  $[\mathbf{w}]_\ell \sim \mathcal{CN}(0, \sigma_w^2)$ , i.e., weights with random phases and magnitudes. In D2.3 [5], we have shown that an improvement of  $1 + c_v^2$  (with  $c_v$  denoting the *coefficient of variation* of the SISO channel power gains  $||[h]_\ell|^2$ ) is achieved on top of that if the channel magnitudes  $||[h]_\ell|$  are deterministically known.

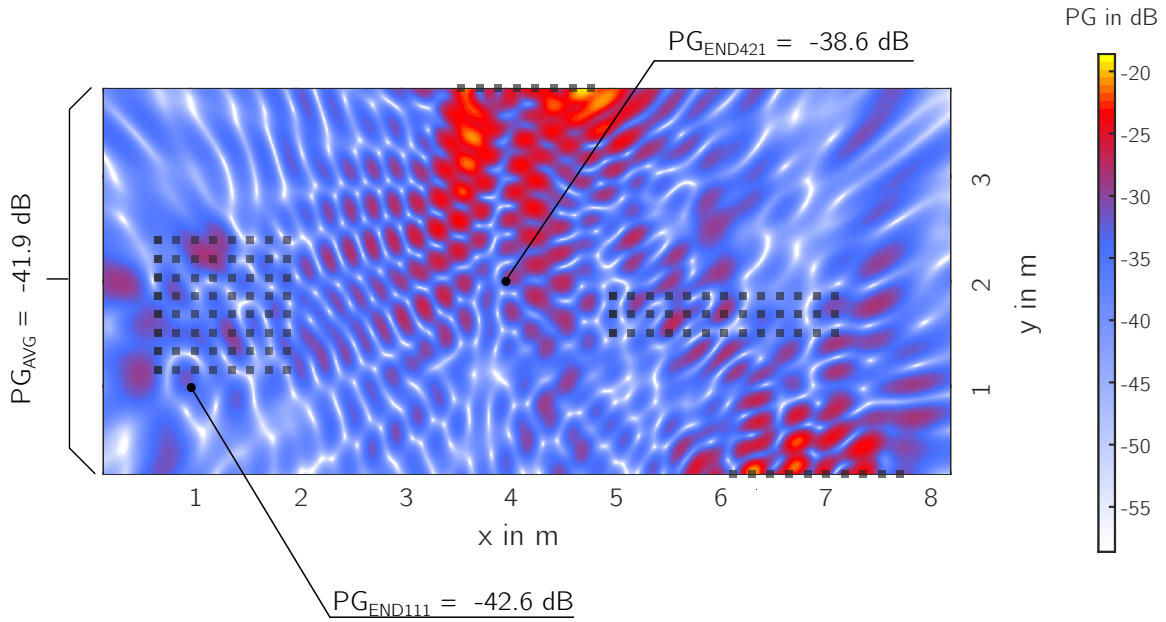


Figure 2.8: Simulated power gain for two END-devices at positions  $[4, 2, 1]^T$  and  $[1, 1, 1]^T$  with a phase error standard deviation of  $180^\circ$ . The average path gain on this plane is  $-41.9$  dB.

By changing the load, the radar cross section (RCS)  $\sigma$  of the backscatter END is altered and signals can be received. The binary sequence of the pilot signal itself typically depends on the chosen DOA-algorithm. In this study, the Multiple Signal Classification (MUSIC)-algorithm is applied, requiring narrow band, discrete-time complex signals. The transmission duration should be chosen high enough for the sample covariance matrix to approach the ideal, array covariance matrix.

### 3. Perform NF-DoA.

As a first exploration, the MUSIC DOA estimator is chosen. This algorithm has been extensively used in different positioning research areas, and thanks to the MIMO-evolution has been shown to achieve a high-resolution application in LTE ([20]) and B5G ([21]) networks. This algorithm introduced by Schmidt in [22] is based on the eigenvalue decomposition of a covariance matrix of an array of sensors, in our case an array of receive antennas. The algorithm uses a matrix of steering vectors for each CSP for a number of azimuth and elevation angles, *i.e.*,  $\mathbf{a}(\phi, \theta)$ . In essence, the algorithm tries to find the best fit of the autocorrelation matrix of these steering vectors (for each pair of azimuth and elevation angles) with the observed sample correlation matrix. While the initial MUSIC algorithm was designed for far field, *i.e.*, planar wavefront, signals, the steering vectors can also be computed using the (array) near-field spherical wavefront.

The general expression for the position estimate by the near-field MUSIC approach is given by,

$$\hat{P}_{\text{MUSIC}}(r, \phi, \theta) = \frac{1}{\mathbf{a}^H(r, \phi, \theta) \mathbf{U}_N \mathbf{U}_N^H \mathbf{a}(r, \phi, \theta)}, \quad (2.19)$$

where  $\mathbf{U}_N$  is the matrix of eigenvectors that span the noise subspace and can be found by the eigenvalue decomposition (EVD) of the sample correlation matrix. The maximum value of Eq. (2.19) can be determined by computing the steering vectors  $\mathbf{a}(r, \phi, \theta)$  for multiple distances

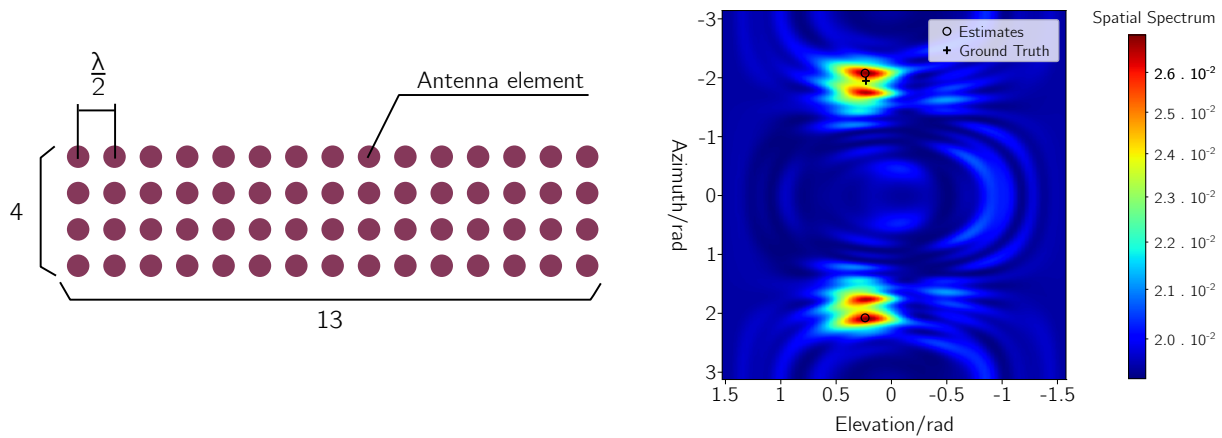


Figure 2.9: The 2D spatial spectrum for the simulated ( $4 \times 13$ ) antenna array in the Tectile environment.

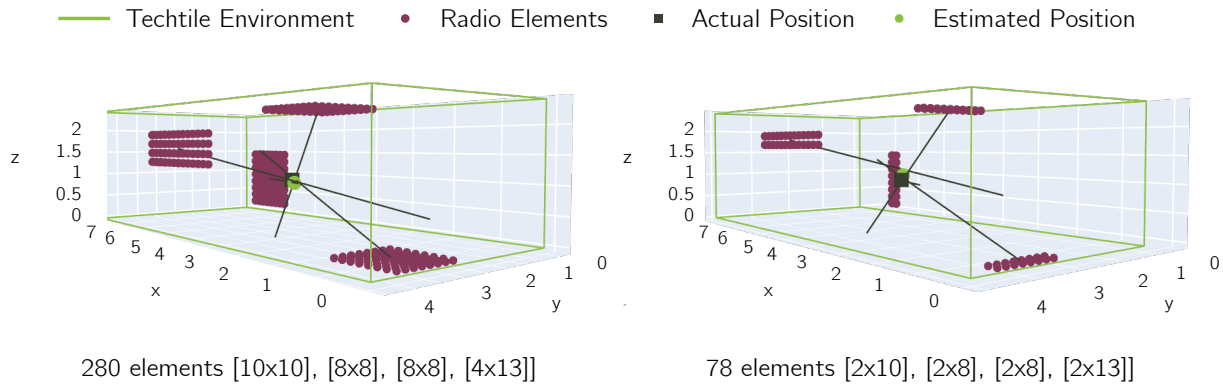


Figure 2.10: 3D DoA estimation plots for the Tectile environment with 280 transceive antenna elements (left) and 78 receive antennae elements (right).

$r$ , azimuth, and elevation angles. An example of the spatial spectrum of this 2D near-field algorithm is given in Fig 2.9 for the ( $4 \times 13$ ) antenna array. The half wavelength antenna-element interspacing is chosen based on the maximum backscatter frequency. That way, all lower frequencies meet the maximum interspacing starting condition of the mathematical model. From this figure, the importance of the geometrical shape of the antenna array can be graphically derived. The smaller number of antenna elements on the vertical axis gives a larger angular error at the azimuth.

Due to the symmetry of the antenna array, two angle estimates are proposed by equation 2.19. Robust angle-of-arrival (AOA) localization methods as applied in [23] can select the appropriate angle for optimal positioning. With these selected azimuth and elevation angles, a simple least-squares 3D positioning estimation can resolve the non-ideal direction vectors to determine a single position estimate. When all 280 antenna elements are used, the calculated Euclidean distance between the actual and estimated position is just above 0.141 m (Fig. 2.10).

The results above are obtained when all 280 elements are considered as transceive antennas. A more realistic approach would divide the antenna-array in transmit and receive sub-arrays. In figure 2.10, the near-field MUSIC algorithm and least-squares positioning estimation are performed

with a receiving antenna subset of only two rows. With these 78 antenna elements, the Euclidean distance between actual and estimated position of the END increases slightly to 0.249 m.

#### 4. Generate power spot.

The last step in this closed-loop approach is to generate the power spot within the MISO channel model described in D4.1 [1]. This power spot should cover a larger volume to counteract the Euclidean distance error of the initial positioning estimate. This larger power spot can be generated through applying a spatial window which is known to suppress sidelobes and widen the main lobe (i.e., the power spot). The planar wavefront beamformer in Section 2.1.1.1 represents a simple and rather inefficient method to widen the focal spot. Other methods involve iteratively constructing beamforming vectors until a certain spatial region is covered [24], or by means of convex optimization [25].

The generation of this power spot results in two effects that both decrease the charge time at the END: (i) it increases the path gain and resulting received power and (ii) it facilitates the END to disable the local oscillator necessary in the mixing process. This latter is visually explained by Figure 3.1 in D4.1 [1], where power density at the carrier frequency is small at the antenna transmit and receive elements. The compressed carrier frequency results in more prominent information signals and counter the need to perform frequency shifted backscattering.

To increase the closed-loop system accuracy, steps 2 to 4 can be repeated in combination with Kalman filtering. Note that when the pilot signals are missing or when new nodes are added to the system, the closed-loop approach should be restarted from step 1.

It can be concluded that for one-time powering purposes, the measurement-based reciprocity beamforming, without calculating the DOA, is a far more efficient method. However, a geometry-based method may benefit from a combination with signal processing methods to widen the power spot. Other ENDS in the close proximity can be powered and even moving devices can be tracked and powered. Another advantage is that the actual, physical position of the END can be calculated, which has great potential from an application point-of-view, aiding in safety, performance, experience and convenience improvements for several use cases. In this section, the adapted near-field MUSIC algorithm offers already a viable Euclidean distance error below 25 cm. Research and comparison with other well-established DOA methods should potentially decrease this distance. Positioning error bounds for a RadioWeaves infrastructure will be derived in the REINDEER deliverable D3.3 [4].

## Chapter 3

# Signal processing for backscatter-based communication

There are several network infrastructure setups that can be used for backscatter communication (BC) with IoT nodes/EN devices. One of them is a bistatic setup where there is a need for high dynamic range and high-resolution analog-to-digital converters at the reader side. In this chapter, we investigate a bistatic BC setup with RW panels. We propose a novel algorithm to suppress direct link interference (DLI) between the carrier emitter (CA) and the reader using beamforming into the nullspace of the CA-reader direct link to decrease the required dynamic range of the system and increase the detection performance of the EN device. Further, we derive a Neyman-Pearson (NP) test and an exact closed-form expression for its performance in the detection of the EN device. Finally, simulation results show that the required dynamic range of the system is significantly decreased and the detection performance of the EN device is increased by the proposed algorithm compared to a system not using beamforming in the CA.

### 3.1 Bistatic backscatter communication

In a BC setup, we usually have the following types of equipment: a CA, a reader, and a backscatter device (BD), e.g., an EN device. The main BC configurations are

- **Monostatic:** In a monostatic BC setup, the CA and the reader are co-located and share many parts of the same infrastructure. For example, the CA and reader either share the same antenna elements or use separate antennas. The CA sends an RF signal to the BD, and the BD modulates the incoming RF signal and backscatters it to the reader [26]. The monostatic system suffers from round-trip path loss, and requires full-duplex technology if the same antennas are simultaneously used for transmission and reception.
- **Bistatic:** In a bistatic BC setup, the CA and reader are spatially separated from each other, and therefore do not typically share RF circuitry, which is beneficial for a number of reasons [27]. For example, the CA and reader can be located separately to decrease the round-trip path loss.
- **Ambient:** In an ambient BSC system, the CA and reader are separated in a similar way as in a bistatic system. However, the ambient system does not have a dedicated CA and uses ambient RF sources such as Bluetooth, Wi-Fi, or TV signals [26].

In a bistatic BC setup, the backscattered signal is weak compared to the DLI due to the double path-loss effect on the two-way backscatter link as seen in Fig. 3.1. That is why the dynamic range of the reader, which is proportional to the signal strength ratio between the received signal from direct link and the weak backscattered signal [28], should be high. As a result, a high resolution ADC is required to detect the weak backscattered signal under heavy interference. In multiple antenna technology, high resolution ADCs are one of the major power consumers [29]. Moreover, the backscattered signal is pushed to the last bits of ADC due to the interference which causes a low signal-to-interference-plus-noise ratio (SINR) [28]. Therefore, it would be beneficial if the DLI is suppressed before the automatic gain control and ADC in order to decrease the required dynamic range of the system.

The authors of [28] investigate the coverage region for narrowband IoT and LoRa technologies considering the receiver sensitivity level, and the effect of the DLI on the dynamic range in the bistatic BC and ambient BC systems. They show that the high dynamic range limits the system performance. In [30] and [31], the carrier frequency of the reflected signal is changed at the END to solve the DLI problem in a SISO bistatic BC system. In [32], the authors apply Miller coding at the END and utilize the periodicity of the carrier signal to mitigate the DLI in a SISO bistatic BC setup. However, the proposed method cancels the interference after the ADC which does not address the high-resolution ADC/high dynamic range problem.

We investigate the bistatic setup with RW panels. Our work can be summarized as follows:

- To address the dynamic range problem in a bistatic BC, we propose a transmission scheme to suppress the DLI by adapting the transmission from the CA using beamforming.
- We derive the optimal NP test to detect the EN device.
- We provide an exact closed-form expression for the performance of the NP test, and analyze the performance of the EN device detection at the reader in a bistatic BC setup with multiple antennas.

## 3.2 Proposed Transmission Scheme

In this section, we present the system model of our bistatic communication setup in Fig. 3.1. We also explain the channel estimation phase and EN device detection phase.

In Fig. 3.1, RW Panel A (PanA) with  $M$  antennas is the carrier emitter, RW Panel B (PanB) with  $N$  antennas is the reader, and EN device C has a single antenna. The EN device can change its reflection coefficient by varying the impedance of the load connected to the EN device antenna to modulate the backscattered signal. Our aim is to decrease the dynamic range of the system, and detect the presence of the EN device. In Phase 1 (P1), we estimate the channel between PanA and PanB. In Phase 2 (P2), we construct a beamformer using a projection matrix which is designed based on the estimated channel to decrease the dynamic range and increase the detection performance by suppressing the interference due to the direct link PanA  $\rightarrow$  PanB.

In Fig. 3.1,  $\mathbf{g}_{AC}^T$ ,  $\mathbf{g}_{CA}$ ,  $\mathbf{g}_{CB}$ ,  $\mathbf{g}_{BC}^T$ ,  $\mathbf{G}_{AB}$ , and  $\mathbf{G}_{BA}$  stand for the channels from PanA to EN device, EN device to PanA, EN device to PanB, PanB to EN device, PanA to PanB, and PanB to PanA, respectively. Here, the dimensions of  $\mathbf{g}_{AC}$ ,  $\mathbf{g}_{CA}$ ,  $\mathbf{g}_{CB}$ ,  $\mathbf{g}_{BC}$ , and  $\mathbf{G}_{AB}$  are  $M \times 1$ ,  $M \times 1$ ,  $N \times 1$ ,  $N \times 1$ , and  $N \times M$ , respectively. We have assumed that PanA and PanB are jointly reciprocity-calibrated such that  $\mathbf{G}_{AB} = \mathbf{G}_{BA}^T$ .

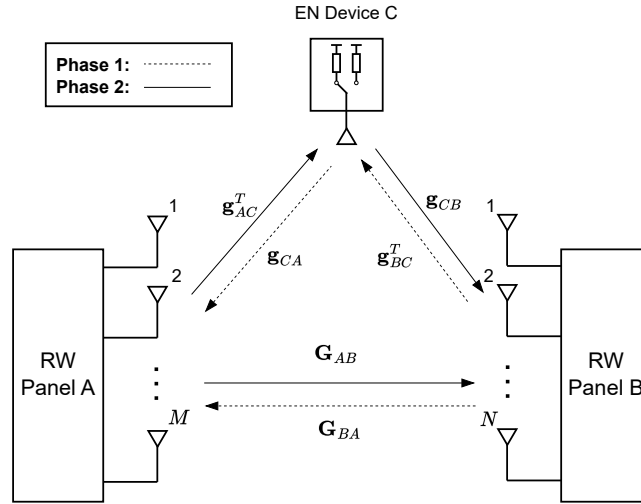


Figure 3.1: The system model of the multi-antenna bistatic backscatter communication.

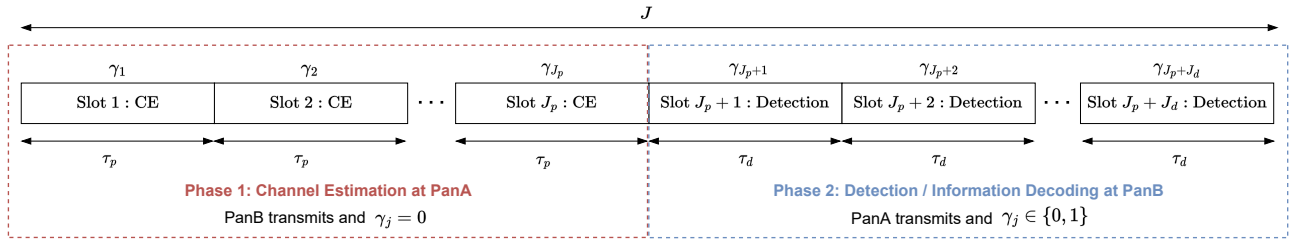


Figure 3.2: The transmission scheme of the bistatic setup.

In Fig. 3.2, the transmission scheme of the considered bistatic communication setup is given. There are two phases, as explained in the next subsections.

### 3.2.1 Phase 1: Channel Estimation at PanA

The first phase comprises  $J_p$  slots ( $\tau_p J_p$  symbols). In each slot, PanB sends the same  $N$  orthogonal pilot signals which each have  $\tau_p$  symbols in order to facilitate estimation of  $\mathbf{G}_{BA}$  at PanA. The symbol length in seconds is denoted as  $L$ , so each orthogonal pilot signal has a length of  $\tau_p L$  seconds. The orthogonal pilot signals sent in a slot are written in matrix form as  $\Phi \in \mathbb{C}^{N \times \tau_p}$ . Here, the pilot matrix  $\Phi$  satisfies  $\Phi \Phi^H = \frac{p_t \tau_p L}{N} \mathbf{I}_N$  and  $\tau_p \geq N$ , where  $p_t$  stands for the transmit power. The total amount of transmitted energy during P1 is expressed as  $E_p \triangleq J_p \|\Phi\|^2 = J_p p_t \tau_p L$ .

In P1, we select the reflection coefficients  $\gamma_j = 0$  for  $j = 1, 2, \dots, J_p$ , i.e., the EN device is silent in each slot. Here,  $\gamma_j$  represents the relative reflection coefficient. When the EN device is silent, its reflection coefficient is a part of  $\mathbf{G}_{BA}$  like other scattering objects in the environment, and the contribution of the backscattered signal to the direct link is negligible. When  $\gamma_j = 1$ , the relative difference in the channel is  $\mathbf{g}_{CA} \mathbf{g}_{BC}^T$ . It is also possible to design an EN device that absorbs the incoming signal for energy harvesting during  $\gamma_j = 0$  [33]. Moreover, in the literature, several papers use on-off keying modulation with two states as used in this paper:  $\gamma_j \neq 0$  and  $\gamma_j = 0$  [33]–[35].

Table 3.1: Mathematical Notations

Parameter	Notation	Dimension
Received signal at PanB	$\mathbf{Y}_j$	$N \times \tau_d$
Received signal at PanA	$\mathbf{Y}_j^p$	$M \times \tau_p$
Channel from PanA to PanB	$\mathbf{G}_{AB}$	$N \times M$
Channel from PanB to PanA	$\mathbf{G}_{BA}$	$M \times N$
Channel from PanA to EN device	$\mathbf{g}_{AC}^T$	$1 \times M$
Channel from EN device to PanA	$\mathbf{g}_{CA}$	$M \times 1$
Channel from EN device to PanB	$\mathbf{g}_{CB}$	$N \times 1$
Channel from PanB to EN device	$\mathbf{g}_{BC}^T$	$1 \times N$
Projection matrix	$\mathbf{P}$	$M \times M$
Probing signal	$\Psi$	$M \times \tau_d$
Additive Gaussian noise at PanB	$\mathbf{W}_j$	$N \times \tau_d$
Additive Gaussian noise at PanA	$\mathbf{W}_j^p$	$M \times \tau_p$
Pilot signal	$\Phi$	$N \times \tau_p$
Reflection coefficient at EN device	$\gamma_j$	$1 \times 1$

### 3.2.2 Phase 2: Detection at PanB

The second phase consists of  $J_d$  slots ( $\tau_d J_d$  symbols). In each slot, PanA sends a probing signal to detect the presence of the EN device at PanB. The probing signal sent in a slot is represented in matrix form as  $\Psi \in \mathbb{C}^{M \times \tau_d}$ , where  $\Psi \Psi^H = \alpha \mathbf{I}_M = \frac{p_i \tau_d L}{M} \mathbf{I}_M$ ,  $\tau_d \geq M$ .

The received signal of dimension  $N \times \tau_d$  at PanB, in slot  $j$  can be written as

$$\mathbf{Y}_j = \mathbf{G}_{AB} \mathbf{P}_s \Psi + \gamma_j \mathbf{g}_{CB} \mathbf{g}_{AC}^T \mathbf{P}_s \Psi + \mathbf{W}_j, \quad (3.1)$$

where  $j = J_p + 1, J_p + 2, \dots, J_p + J_d$  and  $J_p + J_d = J$ . We assume that all the channels are time-invariant during the  $J$  slot durations, i.e., the coherence time of all the channels exceeds  $J$  slots.  $\mathbf{P}_s \in \mathbb{C}^{M \times M}$  is the scaled projection matrix introduced in order to minimize the DLI between PanA and PanB; the design principles for it will be explained in Section 3.3.  $\mathbf{W}_j \in \mathbb{C}^{N \times \tau_d}$  stands for the additive Gaussian noise and each element of  $\mathbf{W}_j$  is independent and identically distributed (i.i.d.)  $\mathcal{CN}(0, N_0)$ , where  $N_0$  is the variance of the noise.  $\gamma_j \in \{0, 1\}$  denotes the reflection coefficients in the EN device, and  $\gamma_j$  can be changed by varying the impedance of the load connected to the EN device antenna. The dimensions of the quantities in the model are summarized in Table 3.1. In Eq. (3.1),  $\mathbf{G}_{AB} \mathbf{P}_s \Psi$  stands for the DLI. The dynamic range of the signal received during P2 is

$$\zeta = E \left\{ \frac{\|\mathbf{G}_{AB} \mathbf{P}_s \Psi\|^2 + \|\mathbf{g}_{CB} \mathbf{g}_{AC}^T \mathbf{P}_s \Psi\|^2}{\|\mathbf{g}_{CB} \mathbf{g}_{AC}^T \mathbf{P}_s \Psi\|^2} \right\}, \quad (3.2)$$

where the expectation is taken with respect to random channel estimation errors (which affect  $\mathbf{P}_s$ ); the channels here are considered fixed. When there is no projection, i.e.,  $\mathbf{P}_s = \mathbf{I}_M$ , the dynamic range can be large:  $\zeta \gg 1$ . When  $\zeta \gg 1$ , we need high-resolution ADCs which are not energy and cost efficient. Moreover, due to the high DLI, the system has low SINR, and the backscattered signal is pushed to the last bits of the ADCs. The scaled projection matrix,  $\mathbf{P}_s \in \mathbb{C}^{M \times M}$ , to the nullspace of the dominant directions of  $\mathbf{G}_{AB}$  (or more exactly, an estimate of  $\mathbf{G}_{AB}$ ) is used to decrease the interference due to the direct link PanA  $\rightarrow$  PanB. As a result, the dynamic range requirements on the reader circuitry decreases.

The next section explains our proposed algorithm to suppress the direct link interference and decrease the dynamic range.

### 3.3 Proposed Interference Suppression Algorithm

In this section, we first present the channel estimation algorithm in P1 for the direct link between PanB and PanA. Then, we propose a novel algorithm based on the estimated direct link channel to mitigate the DLI at PanB in P2. The proposed algorithm decreases the required dynamic range of the system, and increases the SINR and the detection performance. In practice, it also enables the use of low-resolution ADCs due to the decreased required dynamic range.

#### 3.3.1 Channel Estimation at PanA

In this subsection, we present the algorithm to estimate the channel from PanB to PanA,  $\mathbf{G}_{BA}$ .

In the channel estimation phase, PanB sends the same pilot signal  $\Phi$  in each slot. At PanA, the received pilot signal in slot  $j$  is given by

$$\mathbf{Y}_j^p = \mathbf{G}_{BA}\Phi + \gamma_j \mathbf{g}_{CA} \mathbf{g}_{BC}^T \Phi + \mathbf{W}_j^p, \quad (3.3)$$

where  $j = 1, 2, \dots, J_p$  and  $\mathbf{W}_j^p \in \mathbb{C}^{M \times \tau_p}$  stands for the additive noise and all elements of  $\mathbf{W}_j^p$  are i.i.d.  $\mathcal{CN}(0, N_0)$ . We select the reflection coefficients  $\gamma_j = 0$  for  $j = 1, 2, \dots, J_p$ , i.e., the EN device is silent. As a result, Eq. (3.3) can be simplified as

$$\mathbf{Y}_j^p = \mathbf{G}_{BA}\Phi + \mathbf{W}_j^p. \quad (3.4)$$

The channel  $\mathbf{G}_{BA}$  is estimated by least-squares as follows:

$$\hat{\mathbf{G}}_{BA} = \frac{1}{J_p} \sum_{j=1}^{J_p} \mathbf{Y}_j^p \Phi^H (\Phi \Phi^H)^{-1}. \quad (3.5)$$

Due to the reciprocity, the channel  $\mathbf{G}_{AB}$  is simply  $\mathbf{G}_{AB} = \mathbf{G}_{BA}^T$ ; the same holds for their estimates:  $\hat{\mathbf{G}}_{AB} = \hat{\mathbf{G}}_{BA}^T$ .

#### 3.3.2 Interference Suppression Algorithm

This subsection explains our proposed algorithm to decrease the dynamic range and mitigate the DLI at PanB in P2. Based on the channel estimation in P1, PanA designs the projection matrix  $\mathbf{P}$  to minimize the interference at PanB. The required dynamic range of the system is decreased and the performance of the detection of EN device is improved at PanB.

The singular value decomposition of  $\hat{\mathbf{G}}_{AB}$  can be written as

$$\hat{\mathbf{G}}_{AB} = \mathbf{U} \Delta \mathbf{V}^H, \quad (3.6)$$

where  $\mathbf{U} \in \mathbb{C}^{N \times K_0}$  and  $\mathbf{V} \in \mathbb{C}^{M \times K_0}$  are semi-unitary matrices, and  $K_0 \leq \min\{M, N\}$  is the rank of  $\hat{\mathbf{G}}_{AB}$ .  $\Delta$  is a  $K_0 \times K_0$  diagonal matrix with positive diagonal elements ordered in decreasing order.

In P2, PanA transmits a probing signal for PanB to detect the presence of the EN device. The probing signal,  $\Psi$ , satisfies  $\Psi\Psi^H = \alpha\mathbf{I}_M$ . Before transmitting  $\Psi$ , PanA first designs a projection matrix,  $\mathbf{P}$ , based on the channel estimation in P1 in order to decrease the interference at PanB due to the direct link PanA  $\rightarrow$  PanB. After that, PanA projects the probing signal onto the nullspace of  $\hat{\mathbf{G}}_{AB}$  in order to minimize the interference, decrease the dynamic range, and increase the detection probability of EN device at PanB. After the projection, PanA transmits the following signal

$$\mathbf{P}_s\Psi = \sqrt{\frac{M}{M-K}}\mathbf{P}\Psi, \quad (3.7)$$

where  $\mathbf{P}$  is an orthogonal projection of dimension  $M \times M$  and rank  $M - K$ , and  $\sqrt{\frac{M}{M-K}}$  is used to keep the total radiated energy the same during P2 after the projection as follows  $E_d \triangleq J_d\|\Psi\|^2 = J_d\|\mathbf{P}_s\Psi\|^2$ . We select  $\mathbf{P}$  to project onto the orthogonal complement of the space spanned by the columns of  $\mathbf{V}_K$ :

$$\mathbf{P} = \mathbf{I} - \mathbf{V}_K\mathbf{V}_K^H, \quad (3.8)$$

where  $\mathbf{V}_K$  contains the first  $K$  columns of  $\mathbf{V}$  in Eq. (3.6). A suitable value of  $K$  is determined by various factors, such as the number of antennas on the panels, panel shapes like uniform linear arrays or rectangular linear arrays, SNR, and channel model. When there is a strong LoS link and specular multipath components,  $K = 1$  can eliminate the LoS link and reduce the dynamic range. If  $K$  is increased, the dynamic range will continue to decrease as the SMCs are canceled, but the coverage area will also decrease due to the increasing nulls in the antenna radiation pattern. Therefore, it is crucial to choose an appropriate value for  $K$  which can be determined by considering the number of dominant singular values of  $\mathbf{G}_{AB}$  and/or a predetermined dynamic range requirement.

Note that, in order to prevent reducing the power of the backscatter link,  $\mathbf{g}_{CB}\mathbf{g}_{AC}^T$  should not lie in the subspace spanned by the dominant right singular vectors of  $\mathbf{G}_{AB}$ . For example, when  $\text{rank}(\mathbf{G}_{AB}) = 1$  in line-of-sight conditions, the proposed algorithm requires that the CE, BD, and reader should not be located on a line, i.e.,  $\mathbf{g}_{CB}\mathbf{g}_{AC}^T \neq \rho\mathbf{G}_{AB}$  for all  $\rho \in \mathbb{C}$ .

In summary, the received signals during both phases are given by

$$\mathbf{Y}_j^p = \mathbf{G}_{BA}\Phi + \mathbf{W}_j^p, j \in \{1, \dots, J_p\} \quad (3.9a)$$

$$\mathbf{Y}_j = \mathbf{G}_{AB}\mathbf{P}_s\Psi + \gamma_j\mathbf{g}_{CB}\mathbf{g}_{AC}^T\mathbf{P}_s\Psi + \mathbf{W}_j, j \in \{J_p + 1, \dots, J\} \quad (3.9b)$$

### 3.4 Detection of the EN device

In this section, we provide the optimal NP test and analyze its performance for the detection of the EN device in P2. The detection of the EN device at PanB is also equivalent to a binary modulation scheme with the alphabet which has two values “0” and “1”. This problem is formulated as a hypothesis testing problem where the scenarios conditioned on the absence and presence of the EN device are taken as  $\mathcal{H}_0$  and  $\mathcal{H}_1$ , respectively:

$$\begin{aligned} \mathcal{H}_0 : \mathbf{Y}_j &= \mathbf{G}_{AB}\mathbf{P}_s\Psi + \mathbf{W}_j \\ \mathcal{H}_1 : \mathbf{Y}_j &= \mathbf{G}_{AB}\mathbf{P}_s\Psi + \gamma_j\mathbf{g}_{CB}\mathbf{g}_{AC}^T\mathbf{P}_s\Psi + \mathbf{W}_j, \end{aligned} \quad (3.10)$$

where  $j \in \mathcal{S} = \{J_p + 1, \dots, J\}$ . We assume that the receiver has perfect CSI, i.e.,  $\mathbf{G}_{AB}$ ,  $\mathbf{g}_{CB}$  and  $\mathbf{g}_{AC}$  are known. We also assume that  $\Psi$  and  $\mathbf{P}_s$  are known by the receiver.

We apply the optimal NP test to detect the presence of the EN device as follows:

$$L = \frac{\prod_{j \in \mathcal{S}} p(\mathbf{Y}_j | \mathcal{H}_1)}{\prod_{j \in \mathcal{S}} p(\mathbf{Y}_j | \mathcal{H}_0)} \underset{\mathcal{H}_0}{\overset{\mathcal{H}_1}{\geq}} \eta, \quad (3.11)$$

where  $\eta$  is the detection threshold. Here, the NP detector will decide  $\mathcal{H}_1$ , if the likelihood ratio,  $L$ , is bigger than  $\eta$ .  $p(\mathbf{Y}_j | \mathcal{H}_1)$  and  $p(\mathbf{Y}_j | \mathcal{H}_0)$  denote the probability density functions of the observations under  $\mathcal{H}_1$  and  $\mathcal{H}_0$ , respectively, and are given as

$$p(\mathbf{Y}_j | \mathcal{H}_1) = \frac{1}{(\pi N_0)^{N\tau_d}} \exp \left[ -\|\mathbf{Y}_j - \mathbf{G}_{AB} \mathbf{P}_s \Psi - \gamma_j \mathbf{g}_{CB} \mathbf{g}_{AC}^T \mathbf{P}_s \Psi\|^2 / N_0 \right], \quad (3.12a)$$

$$p(\mathbf{Y}_j | \mathcal{H}_0) = \frac{1}{(\pi N_0)^{N\tau_d}} \exp \left[ -\|\mathbf{Y}_j - \mathbf{G}_{AB} \mathbf{P}_s \Psi\|^2 / N_0 \right]. \quad (3.12b)$$

Let define  $\mathbf{A}_j = \gamma_j \mathbf{g}_{CB} \mathbf{g}_{AC}^T \mathbf{P}_s \Psi$  and  $\mathbf{Y}'_j = \mathbf{Y}_j - \mathbf{G}_{AB} \mathbf{P}_s \Psi$ . We can write  $\log(L)$  as follows:

$$\log(L) = - \sum_{j \in \mathcal{S}} \|\mathbf{Y}_j - \mathbf{G}_{AB} \mathbf{P}_s \Psi - \gamma_j \mathbf{g}_{CB} \mathbf{g}_{AC}^T \mathbf{P}_s \Psi\|^2 / N_0 + \sum_{j \in \mathcal{S}} \|\mathbf{Y}_j - \mathbf{G}_{AB} \mathbf{P}_s \Psi\|^2 / N_0 \quad (3.13a)$$

$$= - \sum_{j \in \mathcal{S}} \|\mathbf{Y}'_j - \mathbf{A}_j\|^2 / N_0 + \sum_{j \in \mathcal{S}} \|\mathbf{Y}'_j\|^2 / N_0 \quad (3.13b)$$

$$= \sum_{j \in \mathcal{S}} \frac{1}{N_0} \left( 2 \operatorname{Re}\{\operatorname{Tr}\{\mathbf{A}_j \mathbf{Y}'_j{}^H\}\} - \|\mathbf{A}_j\|^2 \right) \quad (3.13c)$$

Finally, we can write the optimal NP test as follows:

$$L' = \sum_{j \in \mathcal{S}} \operatorname{Re}\{\operatorname{Tr}\{\mathbf{A}_j \mathbf{Y}'_j{}^H\}\} \underset{\mathcal{H}_0}{\overset{\mathcal{H}_1}{\geq}} \eta', \quad (3.14)$$

where  $L' = \frac{\log(L) + \sum_{j \in \mathcal{S}} \|\mathbf{A}_j\|^2}{2/N_0}$  and  $\eta' = \frac{\log(\eta) + \sum_{j \in \mathcal{S}} \|\mathbf{A}_j\|^2}{2/N_0}$ .

To determine the detection performance of the NP test, we first find the distribution of the test statistic,  $L'$ , both under  $\mathcal{H}_1$  and  $\mathcal{H}_0$ . We consider that  $\mathbf{G}_{AB}$ ,  $\mathbf{g}_{CB}$ ,  $\mathbf{g}_{AC}$  and  $\mathbf{P}_s$  are deterministic. Under  $\mathcal{H}_1$ , the test statistic is given by

$$L' = \sum_{j \in \mathcal{S}} \operatorname{Re}\{\operatorname{Tr}\{\mathbf{A}_j (\mathbf{A}_j + \mathbf{W}_j)^H\}\} \quad (3.15a)$$

$$= \sum_{j \in \mathcal{S}} \left( \operatorname{Re}\{\operatorname{Tr}\{\mathbf{A}_j \mathbf{W}_j^H\}\} + \|\mathbf{A}_j\|^2 \right) \quad (3.15b)$$

$$= \sum_{j \in \mathcal{S}} \left( \operatorname{Re} \left\{ \sum_{k=1}^N \sum_{l=1}^{\tau_d} \mathbf{A}_{jkl} \mathbf{W}_{jkl}^* \right\} + \|\mathbf{A}_j\|^2 \right), \quad (3.15c)$$

where  $\mathbf{A}_{jkl}$  and  $\mathbf{W}_{jkl}^*$  denote the element in the  $k$ -th row and  $l$ -th column in  $\mathbf{A}_j$  and  $\mathbf{W}_j^*$ , respectively.  $\mathbf{A}_{jkl} \mathbf{W}_{jkl}^*$  is i.i.d.  $\mathcal{CN}(0, |\mathbf{A}_{jkl}|^2 N_0)$ , and the distribution of the test statistic under  $\mathcal{H}_1$  is

$$L' \sim \mathcal{N} \left( \sum_{j \in \mathcal{S}} \|\mathbf{A}_j\|^2, \frac{1}{2} \sum_{j \in \mathcal{S}} \|\mathbf{A}_j\|^2 N_0 \right). \quad (3.16)$$

Under  $\mathcal{H}_0$ , the test statistic is given by

$$L' = \sum_{j \in \mathcal{S}} \operatorname{Re}\{\operatorname{Tr}\{\mathbf{A}_j \mathbf{W}_j^H\}\} \sim \mathcal{N} \left( 0, \frac{1}{2} \sum_{j \in \mathcal{S}} \|\mathbf{A}_j\|^2 N_0 \right). \quad (3.17)$$

In summary,

$$L' \sim \begin{cases} \mathcal{N}(\sum_{j \in \mathcal{S}} \|\mathbf{A}_j\|^2, \frac{1}{2} \sum_{j \in \mathcal{S}} \|\mathbf{A}_j\|^2 N_0) & \text{under } \mathcal{H}_1 \\ \mathcal{N}(0, \frac{1}{2} \sum_{j \in \mathcal{S}} \|\mathbf{A}_j\|^2 N_0) & \text{under } \mathcal{H}_0. \end{cases} \quad (3.18)$$

The probability of detection ( $P_D$ ) and the probability of false alarm ( $P_{FA}$ ) are calculated as

$$P_D = \Pr\{L' > \eta'; \mathcal{H}_1\} = Q\left(\frac{\eta' - \sum_{j \in \mathcal{S}} \|\mathbf{A}_j\|^2}{\sqrt{\frac{N_0}{2} \sum_{j \in \mathcal{S}} \|\mathbf{A}_j\|^2}}\right), \quad (3.19a)$$

$$P_{FA} = \Pr\{L' > \eta'; \mathcal{H}_0\} = Q\left(\frac{\eta'}{\sqrt{\frac{N_0}{2} \sum_{j \in \mathcal{S}} \|\mathbf{A}_j\|^2}}\right). \quad (3.19b)$$

Finally, we can write the following relation between  $P_D$  and  $P_{FA}$  as follows:

$$P_D = Q\left(Q^{-1}(P_{FA}) - \sqrt{2 \sum_{j \in \mathcal{S}} \|\mathbf{A}_j\|^2}\right). \quad (3.20)$$

### 3.5 Numerical Results

In this section, we first provide the simulation parameters and then discuss numerical results. The channels are modeled as line-of-sight channels without multi-path as follows:

$$[\mathbf{G}_{AB}]_{n,m} = [\mathbf{G}_{BA}^T]_{n,m} = \sqrt{\beta_{m,n}} e^{-j \frac{2\pi}{\lambda} d_{m,n}}, \quad (3.21a)$$

$$[\mathbf{g}_{AC}]_m = [\mathbf{g}_{CA}]_m = \sqrt{\beta_m} e^{-j \frac{2\pi}{\lambda} d_m}, \quad (3.21b)$$

$$[\mathbf{g}_{CB}]_n = [\mathbf{g}_{BC}]_n = \sqrt{\beta_n} e^{-j \frac{2\pi}{\lambda} d_n}, \quad (3.21c)$$

where  $m \in \{1, 2, \dots, M\}$ ,  $n \in \{1, 2, \dots, N\}$ , and  $[\mathbf{G}_{AB}]_{n,m}$ ,  $[\mathbf{g}_{AC}]_m$ , and  $[\mathbf{g}_{CB}]_n$  are the  $(n, m)^{\text{th}}$  element of  $\mathbf{G}_{AB}$ ,  $m^{\text{th}}$  element of  $\mathbf{g}_{AC}$ , and  $n^{\text{th}}$  element of  $\mathbf{g}_{CB}$ , respectively. Path-gain coefficients are defined as

$$\beta_{m,n} = \frac{1}{d_{m,n}^2}, \quad (3.22a)$$

$$\beta_m = \frac{1}{d_m^2}, \quad (3.22b)$$

$$\beta_n = \frac{1}{d_n^2}, \quad (3.22c)$$

where  $d_{m,n}$ ,  $d_m$ , and  $d_n$  stand for the path lengths between the  $m^{\text{th}}$  antenna in PanA - the  $n^{\text{th}}$  antenna in PanB, the  $m^{\text{th}}$  antenna in PanA - the EN device, and the  $n^{\text{th}}$  antenna in PanB - the EN device, respectively. We choose a uniform linear array at both PanA and PanB.

We use the following parameters in all simulations:  $L = 5 \times 10^{-6}$  [36, Ch. 8],  $J_d = 2$ ,  $\tau_d = 16$ ,  $J_p = 1$ ,  $\tau_p = 16$ ,  $N_0 = 1$ ,  $M = 16$ ,  $N = 16$ ,  $K = 3$  and  $\lambda = 0.1$  m, where  $\lambda$  denotes the wavelength of the emitted signal. The center of PanA and PanB are located at  $(0, 0)$  and  $(6, 0)$  in meters, respectively. We select  $K = 3$  to design our projection matrix because the singular values of  $\mathbf{G}_{AB}$  are  $[2.3261, 1.2565, 0.3140, 0.0445, 0.0045, \dots]$ , and the projection matrix with  $K = 3$  can

Table 3.2: Simulation Parameters

Parameter	Value
Symbol length in seconds	$L = 5 \times 10^{-6}$
Number of slots for the probing signal	$J_d = 2$
Number of symbols in each slot for the probing signal	$\tau_d = 16$
Number of slots for the pilot signal	$J_p = 1$
Number of symbols in each slot for the pilot signal	$\tau_p = 16$
Number of antennas in PanA	$M = 16$
Number of antennas in PanB	$N = 16$
Number of antennas in EN device	1
The location of PanA, PanB, and EN device in meters	$(0, 0)$ , $(6, 0)$ , and $(3, y)$ , where $y \in [0, 20]$
Inter-antenna distance both in PanA and PanB in meter	$0.5\lambda = 0.05$
Noise variance	$N_0 = 1$
Reflection coefficients at EN device	$\gamma_j = 0$ for $j = 1, \dots, J_p$ and $\gamma_j \in \{0, 1\}$ for $j \in \mathcal{S}$
First $K$ columns of $\mathbf{V}$	$K = 3$
SNR during the detection of EN device	$\text{SNR}_d = -10$ dB
SNR during the channel estimation	$\text{SNR}_p = 0 - 30$ dB

project the transmitted signal onto the nullspace of the dominant directions of  $\mathbf{G}_{AB}$ . We select the reflection coefficients at the EN device as  $\gamma_j = 0$  for  $j = 1, \dots, J_p$  in P1 and  $\gamma_j \in \{0, 1\}$  for  $j \in \mathcal{S}$  in P2, and we have the same number of  $\gamma_j = 0$  and  $\gamma_j = 1$  in P2. The SNR during the estimation of  $\mathbf{G}_{BA}$  in P1 is defined as  $\text{SNR}_p = \bar{\beta}_{BA} p_t J_p \tau_p L / N_0$ , where  $p_t$  and  $L$  are the transmit power and the symbol length in seconds, and  $\bar{\beta}_{BA} = \frac{\|\mathbf{G}_{AB}\|^2}{MN}$ . The SNR during the detection of EN device in P2 is given as  $\text{SNR}_d = \bar{\beta}_{CB} \bar{\beta}_{AC} p_t J_d \tau_d L \bar{\gamma} / N_0$ , where  $\bar{\gamma} = 0.5$  is the average value of the reflection coefficients in P2, and  $\bar{\beta}_{AC} = \|\mathbf{g}_{AC}\|^2 / M$  and  $\bar{\beta}_{CB} = \|\mathbf{g}_{CB}\|^2 / N$ . We list all the simulation parameters in Table 3.2.

In Fig. 3.3, the theoretical and simulation results for the detection performance of the optimal NP test in Eq. (3.14) are given. We used  $10^5$  Monte-Carlo runs for the simulation results. A triangular setup is used and the EN device is located at  $(3, 3)$  in meters. We select  $\text{SNR}_d = -10$  dB, and consider two different scenarios: (1) perfect projection and (2) no projection to investigate the effect of the scaled projection matrix  $\mathbf{P}_s$  on  $P_D$  and  $P_{FA}$ . While  $\mathbf{P}_s = \mathbf{I}_M$  for the no-projection case, the projection matrix is designed based on perfect CSI, i.e.,  $\hat{\mathbf{G}}_{AB} = \mathbf{G}_{AB}$ , by PanA for the perfect-projection case. Since the projection matrices in both scenarios are deterministic, we use Eq. (3.20) to calculate the theoretical curves. In the figure, the theoretical results exactly match with the computer simulation results.

The system which works with perfect projection matrix projects the transmitted signal to the nullspace of the dominant direction of  $\mathbf{G}_{AB}$ . As seen in the figure, the detection performance is better in the case of perfect projection. It is observed because the radiated power in the directions which are close to the dominant direction of  $\mathbf{G}_{AB}$  decreases and the emitted power in all other directions increases. As a result, the received power at PanB from EN device signal increases with an accurate projection matrix. For example, at  $P_{FA} = 0.1$  in Fig. 3.3, the system with perfect projection has almost 0.06 gain in  $P_D$  when compared to the system with no projection.

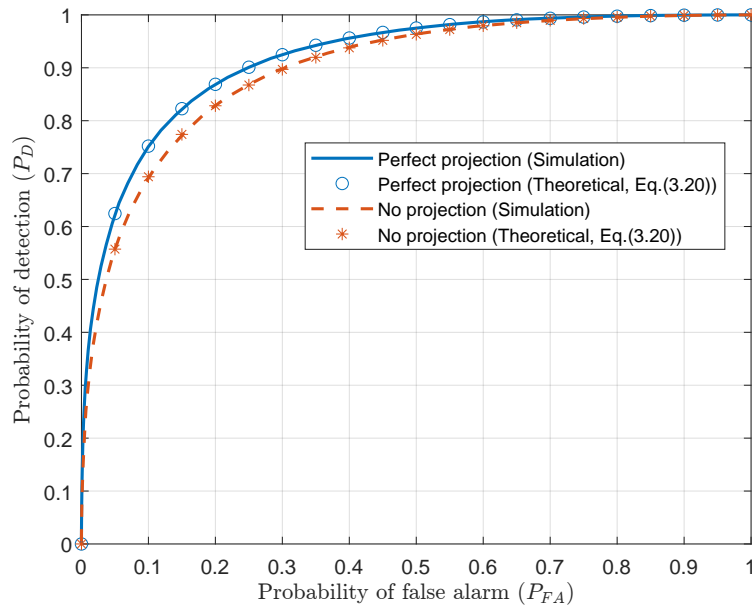


Figure 3.3: The detection performance of EN device at PanB.

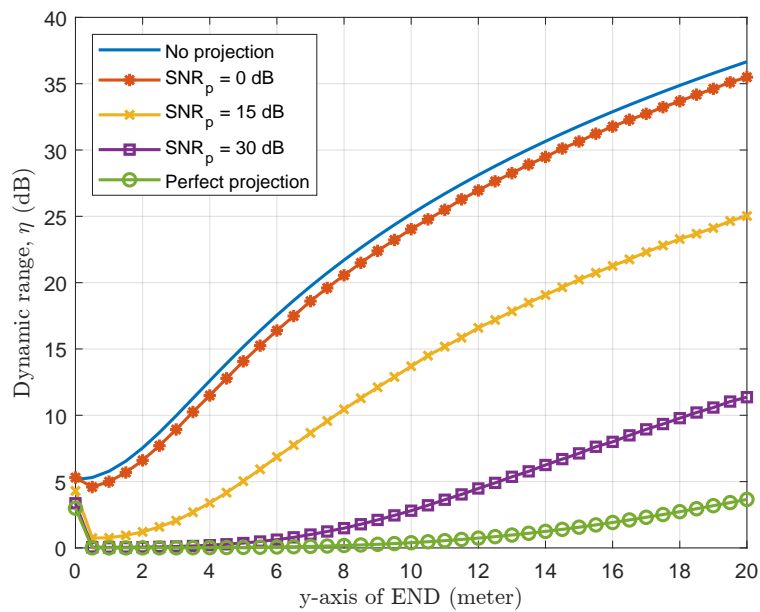


Figure 3.4: The ratio of the backscatter plus direct link power to the backscatter link power.

In Fig. 3.4, we sketch the ratio  $\zeta$  given in Eq. (3.2) for different EN device locations to investigate the change in the dynamic range of the system with and without projection. The center of PanA and PanB are located at  $(0, 0)$  and  $(6, 0)$  in meters, respectively and the EN device is located at  $(3, y)$ , where we change the vertical position of EN device,  $y$ , between 0 and 20 meters. Here, PanA estimates the direct channel using the transmitted pilot signal by PanB in P1. We use  $10^3$  different realizations of the estimated direct channel to obtain Monte-Carlo simulation results. We compare  $\zeta$  for varying  $\text{SNR}_p$  values from 0 dB to 30 dB. As seen in the figure, at  $y = 0$ , the effect of the projection matrix on  $\zeta$  is low, because  $\mathbf{g}_{CB}\mathbf{g}_{AC}^T$  lies mostly in the subspace spanned by the dominant right singular vectors of  $\mathbf{G}_{AB}$ .

In Fig. 3.4, the dynamic range,  $\zeta$ , decreases with increasing  $\text{SNR}_p$  when  $y > 0$  m. This is because the projection matrix designed with high  $\text{SNR}_p$  values has more capability to decrease the interference due to the direct link PanA  $\rightarrow$  PanB. For example, at  $y = 10$  m,  $\zeta$  is 25.17 dB, 23.98 dB, 13.74 dB, 2.83 dB, and 0.39 dB for the no projection,  $\text{SNR}_p = 0$  dB,  $\text{SNR}_p = 15$  dB,  $\text{SNR}_p = 30$  dB, and perfect projection cases, respectively. In practice, with a decreased dynamic range, it is possible to use low-resolution ADCs which are more cost and energy efficient than high-resolution ADCs.

In conclusion, we present a novel transmission scheme to suppress the DLI at the reader in a bistatic BC setup with multiple antennas. We first estimate the channel between the CE (PanA) and the reader (PanB). Using the estimated channel, we design a projection matrix which is then used as a beamformer in order to mitigate the DLI and decrease the required dynamic range of the reader. Further, we derive the NP test assuming perfect CSI and a closed-form expression for its performance for the detection of the END at the reader. We show that the dynamic range of the system is significantly decreased and the detection performance of END at the reader increased by using the projection matrix.

Moreover, a detector design without perfect CSI at the reader is left for future work. If required, the proposed DLI suppression algorithm can also be redesigned considering beam sweeping/beam forming in the initial access to be able to detect transmitted symbols from the END during the initial access phase.

## Chapter 4

# Signaling / Optimal waveform design

Designing an optimal waveform is relevant to improve RF energy harvesting, as it affects RF-to-DC efficiency. By optimizing the waveform design, the efficiency of the energy conversion process can be improved, and more energy can be harvested from the RF signals. Waveforms to ensure RF-to-DC efficiency gains, typically result in high peak-to-average power ratio (PAPR) signals. As the term explains, the signal power level will fluctuate and peaks of higher radiated power will occur periodically. At non-peak times, the transmitted power is remarkably lower than the average radiated power. Although a high PAPR is not always desired in data communications because of the requirements these signals pose to the PA specifically, they can be advantageous in RF power transfer.

This study of alternative waveforms is motivated by the restrictions in radiated power. The REINDEER deliverable D4.1 [1] already explained the regulations in the considered frequency bands. Searching for techniques, e.g., generating different waveforms with an equal radiated power level, which could consequently result in higher energy transfer efficiency, is therefore worth considering. This discussion does not focus on the regulations themselves. This analysis targets a fair comparison between the optimized waveforms and a single tone signal. In order to do so, the generic waveforms should have the same average power as a single tone waveform to investigate potential efficiency gains.

The rectifier circuit is responsible for the RF-to-DC conversion. To show that efficiency gains are achievable, the rectifier circuit must be inspected in more detail. The main electronic component of a rectifier is the diode whose model can typically be represented by Equation (4.1).

$$i_D = I_s \left( e^{\frac{V_D}{nV_T}} - 1 \right) \quad (4.1)$$

Contrary to a capacitor, coil, or resistor, a diode is a non-linear electronic component, which is clear from the previous model. The threshold voltage  $V_T$  must be transcended to achieve an RF-to-DC conversion. Theoretically, higher input amplitudes from the RF source could be converted more efficiently than lower amplitudes due to the fact that the diode losses divided by the overall rectified power decrease at higher amplitude levels. As a result, an optimized input signal can yield efficiency gains.

## 4.1 Supplying multi-sine signal to rectifier circuits

The rectifier circuit itself can be constructed in different ways, where the single diode rectifier and the  $N$ -stage voltage doubler (with  $N$  the number of stages) are common rectifier circuits in RF energy harvesters [37], [38]. In this analysis, we consider the single diode and one-stage voltage doubler.

In general, a single diode rectifier is a circuit that uses a single diode to rectify the RF signal into a direct current (DC) voltage. The single diode only allows current to flow in one direction, effectively converting the alternating current (AC) signal into a pulsed DC signal. This type of rectifier is simple, inexpensive, and efficient for low voltage inputs. However, it only rectifies half of the input AC waveform, producing a lower DC output voltage compared to the voltage doubler rectifier. A voltage doubler rectifier is a circuit that uses two diodes and two capacitors to double the AC voltage by means of using both half cycles, and produce a higher DC output voltage. The voltage doubler rectifier works by rectifying the positive and negative half cycles of the AC signal and storing the energy in the capacitors. It is more efficient for high input power levels compared to a single diode rectifier as described in [37].

The choice between a single diode rectifier and a voltage doubler rectifier for an energy harvester will depend on the specific application and the desired output voltage and efficiency. The question we here focus on is whether both circuits are suitable for input signals that differ from a single tone signal.

To verify this, both rectifier circuits are simulated in Spice combined with a matching circuit. The load is held constant at 10 k $\Omega$ . An RF schottky diode *SMS7630* is selected. The circuits are illustrated in Figures 4.1 and 4.2.

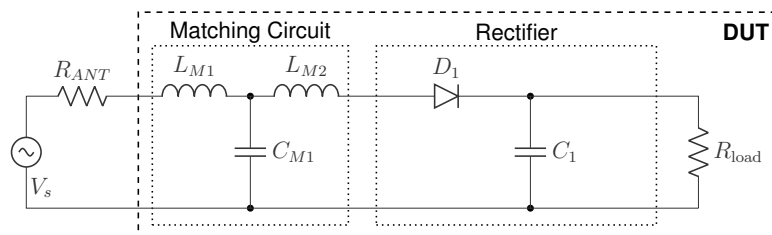


Figure 4.1: Single diode rectifier circuit in PySpice simulations.

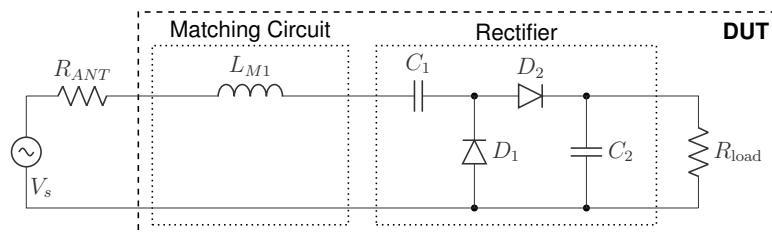


Figure 4.2: One stage voltage doubler rectifier circuit in PySpice simulations.

To reduce the complexity of the simulations, multi-sine signals were constructed and the results were compared with those of single sine continuous wave (CW) signals. In order to automatically sweep over a wide input power range from  $-30$  dBm to 20 dBm, PySpice was used. The rectifier efficiency can be determined by dividing the output power dissipated in  $R_{load}$  by the input power of the rectifier.

In this comparative study, the full harvester efficiency is considered, including matching losses and consequently reflections. Due to the nonlinear model of a diode, it is challenging to match a rectifier circuit. Usually, the input impedance is determined by simulations or measured with a VNA. Based on the obtained complex input impedance and using the Smith chart, an appropriate matching network is proposed. The nonlinear model of the diode causes an additional input power dependency, among the frequency dependency. This additional dependency means that the matching circuit cannot ensure a perfect match over the entire input power range. In Figures 4.1 and 4.2, a matching network for both rectifier circuits is proposed.

The antenna is represented by an AC source combined with an antenna impedance  $R_{ANT}$ . In the calculations and simulations, the antenna impedance is set to  $50\ \Omega$ . Suppose that the antenna (consisting of  $V_s$  and  $R_{ANT}$ ) is perfectly terminated with a  $50\ \Omega$  load and, as an exemplary value, we want to dissipate 0 dBm of power in the terminated load, it is crucial to define the corresponding amplitude that should be applied by the AC source  $V_s$ . Via Equation (4.2), the amplitude magnitude of the frequency peaks of the multi-tone signal is calculated to dissipate an amount of power  $P_{IN}$  in a perfectly matched circuit ( $R_{DUT} = R_{ANT}$ ). Hereby,  $M$  is the number of tones. Similarly, the amplitude for a single tone signal can be determined by taking  $M = 1$ .

$$V_{S,P} = 2 \cdot \sqrt{2} \cdot \sqrt{10^{\frac{P_{IN}[\text{dBm}]}{M \cdot 10}} \cdot 0.001[\text{mW}] \cdot R_{ANT}} \quad (4.2)$$

The overall harvester efficiency consists of the power dissipated in  $R_{load}$  divided by the power dissipated in a perfectly matched antenna ( $R_{DUT} = 50\ \text{ohm}$ ). Several simulations were performed for both rectifier circuits with waveforms consisting of multiple tones for different input power levels.

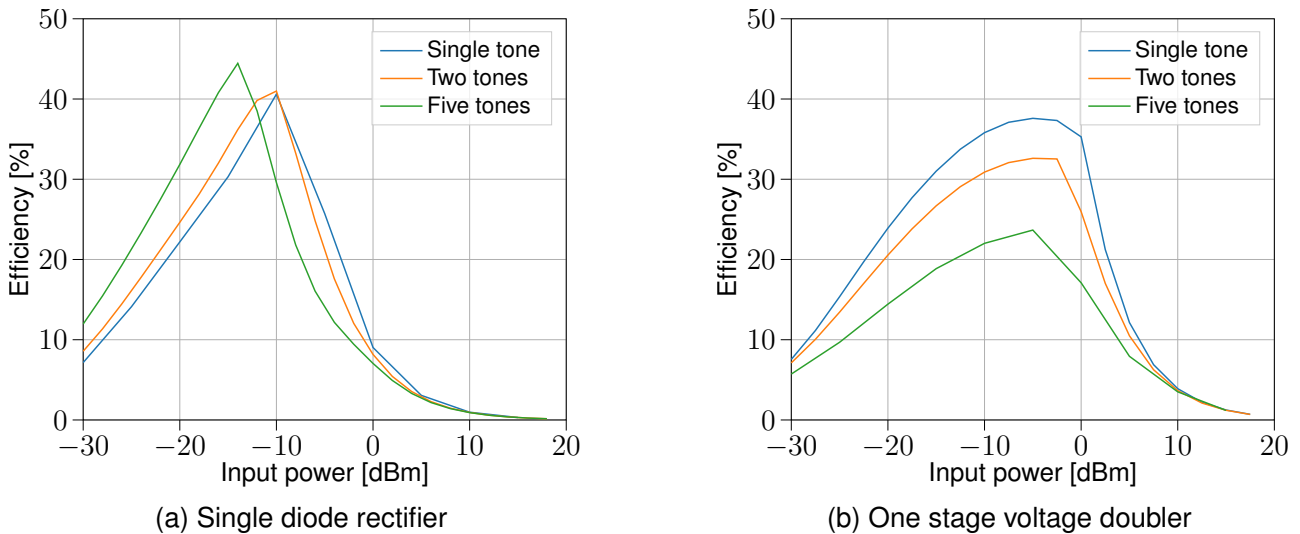


Figure 4.3: Comparison of efficiency for single and multi-sine signals for multiple input powers.

The results from Figure 4.3 show that for the single diode rectifier efficiency gains are achievable with, when  $M$ , the number of frequency components, increases. However, with a voltage doubler, the opposite effect is obtained. It turns out that the voltage doubler performance decreases with increasing frequency components of the multi-sine signal. The clarification for this effect is that the rectifier circuit no longer works as a true doubler.

Despite the fact that several researchers have aimed to increase RF-to-DC efficiency by applying high PAPR signals, it turns out that these signals are not always beneficial for the harvester

performance. [39] has described this phenomenon more in detail specifically for a voltage doubler rectifier.

The single diode rectifier does demonstrate potential efficiency gains with increasing number of sines. In previous simulations, the load was kept constant. However, in real situations, the loads will fluctuate. [40] describes the efficiency by performing a sweep over multiple load values. This analysis shows that a single diode rectifier can convert a single tone signal more efficiently to DC at smaller resistive loads relative to higher resistive values.

## 4.2 Performance with a commercial harvester circuit

To check whether gains could be achieved in current applications, a commercially available harvester was used to measure whether multi-sine signals or higher PAPR signals yield efficiency gains. In this measurement, the evaluation board for the e-peas AEM40940 IC [41] was selected, which operates among others frequencies at 867 MHz. The incoming RF signal was constructed with three sine waves generated by three USRPs and combined with an RF combiner. The strength of the frequency components of the combined signals were measured with a spectrum analyzer to take cable and RF combiner losses into account. Then a single tone signal with the same average power (by applying Parseval's Power Theorem) was evaluated in a similar way.

Measurements with the commercial harvester showed that there are no gains achieved when using multi-sine signals. Table 4.1 shows the results of an experiment where an average power of  $-16$  dBm is supplied at the input of the harvester for both single tone and multi-tone waveforms. The latter is based on three combined sine waves. Our findings show that the efficiency is higher with a single tone signal. In other words, imagine that a manufacturer wants to develop ENDS and select, for example, this harvester, then the RF-DC efficiency will be higher if this harvester receives a signal with one spectral frequency component.

Tone	Peak 867 MHz [dBm]	Peak 868 MHz [dBm]	Peak 869 MHz [dBm]	Total/avg. $P_{\text{supply}}$ [dBm]	DC power [dBm]	Efficiency [%]
Multi	-21.0	-20.2	-21.3	-16.0	-25.4	11.7
Single	0	-16.0	0	-16.0	-23.4	18.3

Table 4.1: RF-to-DC conversion efficiency measurement with the e-peas AEM40940 harvester for both single tone and three-tone input signals.

The measurements with the existing harvester show that it is not necessarily advantageous to feed a harvester circuit with a high-PAPR signal. Also, simulations with a voltage doubler and research reported in [39] show that there is usually no achievable gain by supplying this type of circuit with multi-sine signals. Nevertheless, high PAPR signals are found to be favorable for single-diode rectifier circuits, and can result in efficiency gains.

# Chapter 5

## Optimal hardware design

### 5.1 Introduction

The optimal hardware design for energy harvesting systems is one that maximizes energy conversion efficiency while meeting the specific requirements and constraints of the application. This requires a careful balance between the energy harvesting source, the energy storage, and the power management subsystems. The design should also consider the physical form factor and size constraints, as well as the expected operating environment and conditions.

Additionally, it is important to consider the trade-off between power consumption and data rate, as well as the integration level of the components and subsystems to improve overall performance and efficiency. By considering these factors and utilizing the latest technologies and advancements in the field, an optimal hardware design for energy harvesting systems can be achieved.

### 5.2 Optimal transceiver design

In general, it can be stated that there is no optimal transceiver design in the sense of a global optimum. It heavily depends on the specific use case, the frequency of operation, and the signaling schemes. However, a key goal is to maximize the overall power conversion efficiency along the entire path from the powering antennas of the infrastructure to the end device and back to the receiving antenna of the infrastructure. Of course, there are basic considerations that apply to any optimization strategy for a wireless power harvester. These include:

- Avoiding the use of dedicated lumped element matching networks whenever possible, because real components do have losses. In general, introducing a matching network on the end device can reduce the overall power efficiency by up to 50% (see D4.1 [1] for details).
- Applying broadband antenna matching. End devices, especially RFID tags, are often placed in proximity to or even attached to different types of surfaces that will detune the antenna to some extent. In cases where the antenna design is too narrowband, such detuning may shift the resonance frequency to regions where the power carrier cannot be received, resulting in heavily degraded performance.
- Considering the trade-off between power consumption and data rate when optimizing the transceiver design. In some cases, a higher data rate may be required, but this may come

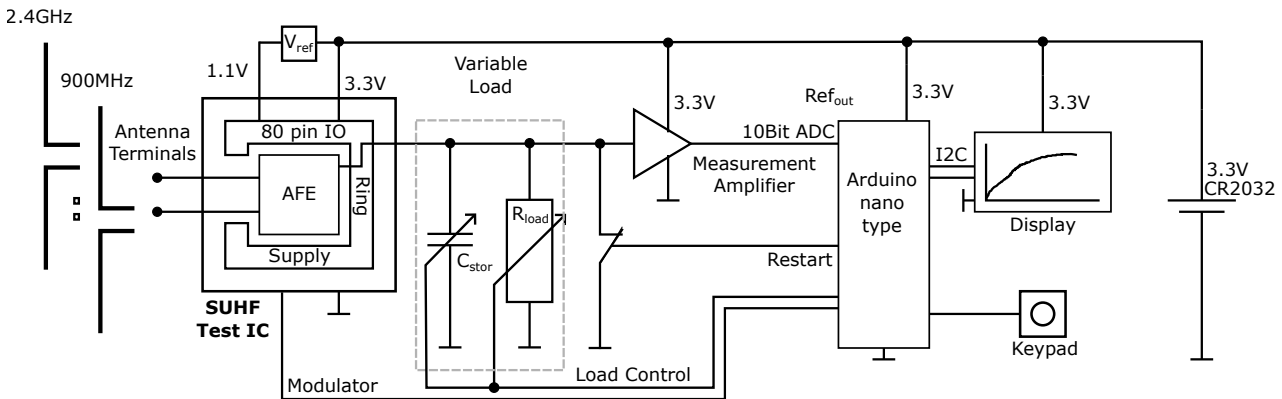


Figure 5.1: Block diagram of the harvesting demonstrator to evaluate different use-cases.

at the cost of increased power consumption. In other cases, low power consumption may be the priority, even if it means a lower data rate.

- Pursuing a high integration level of the components and subsystems in the design of the transceiver. The more that can be integrated onto a single integrated circuit (IC), the higher the overall efficiency can be. This is because integrated circuits can significantly reduce the number of interconnections and passive components, which in turn reduces loss and improves performance. In addition, integrated circuits can also help to minimize the physical size and weight of the transceiver, which is particularly important for portable or mobile devices. Integration can also help to improve the reliability and robustness of the transceiver. By integrating multiple components and subsystems onto a single IC, the number of interconnections and passive components is reduced, which can decrease the probability of failure and improve overall performance. Furthermore, integrated circuits can also help to simplify the transceiver design and reduce the complexity of the system, which can lead to lower costs and faster time-to-market.

In summary, integration of the components and subsystems of the transceiver can significantly improve the overall performance, efficiency, reliability and robustness, as well as reducing the physical size and weight of the device, and simplifying the design process.

Overall, the transceiver design optimization process is a complex task that requires careful consideration of various factors and trade-offs. It is important to consider the specific use case and requirements, as well as the latest technologies and advancements in the field in order to achieve the best possible performance and efficiency.

Therefore, we have developed a harvesting demonstrator. With this demonstrator we want to perform measurement campaigns in different use-case scenarios. The evaluation of the measurements are used to outline the specification of an RF energy harvesting demonstrator operating at different frequencies suitable for the different use-case objectives. Furthermore, by using this demonstrator, it should be possible to account for the achievable array gain ratio, comparing the RadioWeaves performance against conventional harvesting systems.

The basic block diagram is illustrated in Figure 5.1. The core element of the demonstrator is based on a test IC fabricated for this project. It includes an analog front end (AFE), basically a multi-stage charge-pump circuit which is very sensitive. With the specific design it is possible to harvest uWatts of Power by providing sufficient voltage to drive digital logic or an ultra-low power MCU. However, in order to measure the received power in a dynamic scenario, the demonstrator

Table 5.1: Specifications of the Demonstrator Hardware

<b>Specifications</b>	
Target min charge pump current	1 $\mu$ A
ADC resolution	92 $\mu$ V (15 bit/3 V)
Measurement input current sensitivity	10 nA
Charge pump voltage range	0.2 V . . . 2 V
Demonstrator max supply current	20 mA
Sampling rate	8 Hz . . . 128 Hz
Sensitivity	-19 dBm (1.5 V DC out)

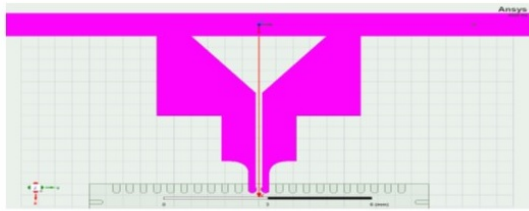
comprises a digital sub-system able of measuring and displaying the instant energy and power levels. The measurement apparatus can also evaluate the energy condition over time and will display the results. It has the ability to configure the DC load dynamically. This will not only show the capabilities and limitations of the current charge-pump implementation, but also will give insight on the amount of instant power available to use to supply different auxiliary circuits. In order to make these features available, the demonstrator requires a battery source to drive the on-board MCU, the display, and the measurement circuit. The test IC also requires voltage supplies (3.3 V and 1.1 V). These voltages are solely necessary to supply the 80 pin IO-ring of the multiplexers and level shifters to control the IC. This would not be necessary when all system would be integrated to the IC. This solution was selected to create the possibility to perform true measurements of the power conversion efficiency of the AFE without considering these additional losses. Overall, it is a handheld device recording the available energy at a specific location or in dynamic situations when moving around. Table Table 5.1 shows the specifications of the demonstrator.

### 5.3 Joint-optimal circuit and antenna design

As mentioned, joint-optimal circuit and antenna design is crucial for achieving maximum energy conversion efficiency. The circuit and antenna design have a strong interdependence, and optimizing one without considering the other can lead to significantly sub-optimal results. One example of a jointly-optimized circuit and antenna design is the use of impedance matching techniques (also described in the REINDEER deliverable D4.1 [1]). Impedance matching is used to optimize the power transfer between the energy harvesting source and the circuit. By carefully designing the circuit and the antenna together, the impedance can be matched at the operating frequency, resulting in maximum power transfer and improved energy conversion efficiency.

Another example is the use of frequency selective surfaces (FSSs) in the antenna design. FSS can be used to selectively reflect or transmit specific frequency bands, which can be exploited to optimize the energy harvesting performance. When combined with a properly designed circuit, FSS can significantly improve the overall energy conversion efficiency. The FSS can be designed to shape the radiation pattern of the receiving antenna by reflecting or transmitting certain frequency bands. This can be useful to enhance the energy received by the antenna in certain directions, and reduce it in others, depending on the requirements of the application. Furthermore, FSS can also provide a way to improve the antenna performance in the presence of obstacles or in a multipath environment, by reflecting or transmitting certain frequency bands in certain directions.

- 2.45GHz antenna design including IC package parasitic



- 915 MHz antenna design IC including package parasitic

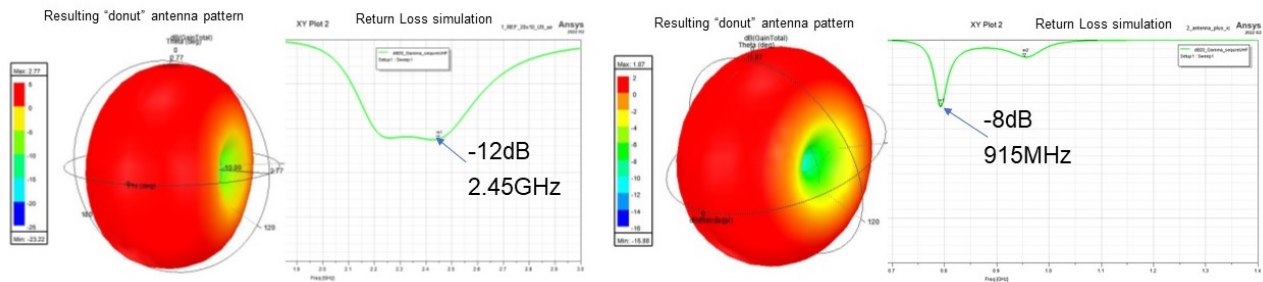
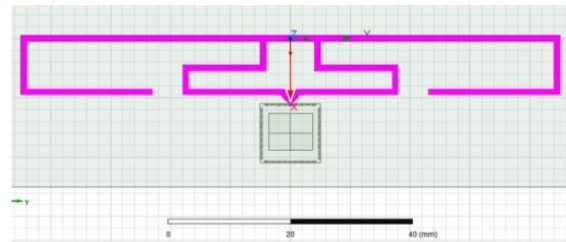


Figure 5.2: Optimal antenna design, two variants: 915 MHz and 2.45 GHz.

In addition, the integration of the circuit and antenna can also play a key role in achieving a joint-optimal design. By integrating the circuit and antenna on the same substrate, the number of interconnections and passive components can be reduced, resulting in improved energy conversion efficiency and simplified design. This is a technique that is attractive for sealed proximity applications in the higher GHz domain.

Overall, the joint-optimal circuit and antenna design is essential for achieving maximum energy conversion efficiency in energy harvesting systems. The circuit and antenna design should be considered together and optimized for the specific operating conditions and requirements in order to achieve the best results.

In this context, two examples on the results of optimal antenna design for the harvesting demonstrator developed here are illustrated in Figure 5.2. It shows two variants: On the left, the 2.45 GHz match is displayed, along with the corresponding antenna pattern and return loss characteristics across the frequency of interest. On the right, the 915 MHz variant is shown, again with the corresponding antenna pattern and return loss. The target antenna pattern is usually selected to be omnidirectional (or at least exhibit dipole characteristics) because there should not be any restriction on the position or orientation of the EN device. The final return loss characteristic is a part of the optimization procedure. The theoretical considerations regarding the optimal matching procedure are described in D4.1 [1]. However, two important parameters have to be determined. One is the parasitic impedance of the IC terminals (including package, terminal pins, cross-coupling, and wire bonding between the pins and the silicon landing pads). The second parameter is the nominal impedance of the charge-pump. The latter typically is the value at which maximum sensitivity shall be achieved. These two parameters are usually obtained by simulations supported with reference measurements.

In order to perform rapid prototyping, the antennas are usually fabricated with additional tuning stubs. Implementations related to the harvesting demonstrator are illustrated in Figure 5.3. The amount of tuning has to be evaluated by measurements in an anechoic chamber. Here the frequency of operation will be swept across the frequency bands of interest. In case the target frequency is not at its maximum, the tuning stubs have to be cut at distinct position found by iteration.

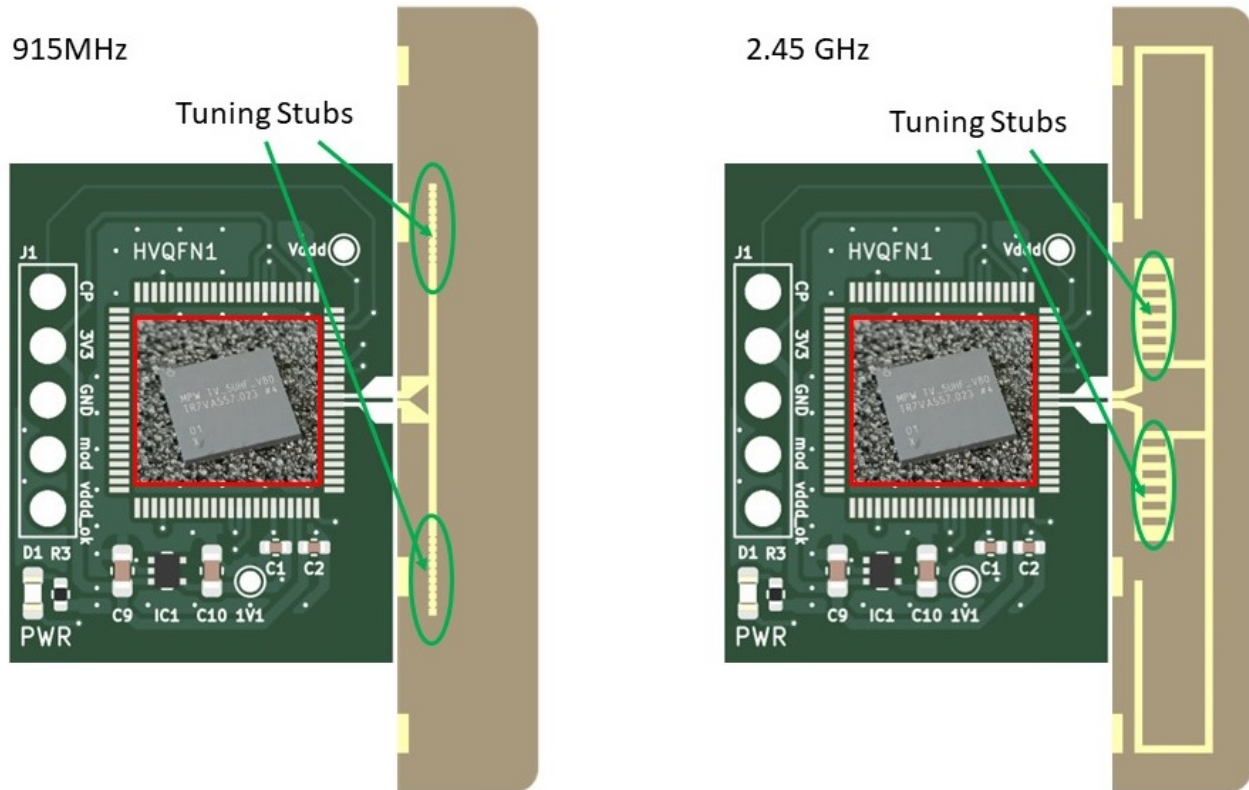


Figure 5.3: Optimal antenna design, two variants: 915 MHz and 2.45 GHz, fabricated with additional tuning stubs.

As outlook and next steps, we want to evaluate the performance of the device in the anechoic chamber to establish a ground truth in terms of achievable distance, possible instant power levels and efficiency. The evaluation will be done solely in a SISO setup. Then, we want to evaluate the performance in specific use-cases and finally we want to quantify the achievable gain in RadioWeaves infrastructure.

# Chapter 6

## Summary

This deliverable demonstrated a range of signal processing methods that facilitate the achievable array gains of a RadioWeaves infrastructure: We presented geometry-based beamformers that predict channel state information (CSI) based on geometric environment information and thereby exploiting environment awareness. We evaluate their performance on synthetic aperture measurements and compare them against a measurement-based beamformer subject to noisy CSI. We additionally revealed the limits of random beamforming (also known as opportunistic beamforming). Fusing both measurement-based and geometry-based CSI of an environment-aware infrastructure, we demonstrate a closed-loop approach that successively optimizes beamforming weights to gain improved CSI by exploiting the wireless positioning feature of a RadioWeaves infrastructure. Our evaluation based on synthetic aperture channel measurements demonstrates that the achievable gains of physically large apertures operating at sub-10 GHz can lift the receivable power at the device side from the microwatt to the milliwatt range while transmitting over distances greater than 10 meters.

A RadioWeaves infrastructure benefits from massive deployments of antennas leveraging array gains and diversity. Our beamforming scheme for bistatic backscatter communication demonstrates how beamforming weights can be designed to decrease the necessary dynamic range (and power consumption) of the infrastructure and increase the detection performance of energy neutral (EN) devices. Utilizing simulations, we can demonstrate significant gains by exploiting *spatial diversity*. This allows us to use low-resolution ADCs which are low-cost and more energy-efficient than high-resolution ones.

In Chapter 2, we were focusing on the RF-to-RF efficiency of the system with a particular focus on geometric modeling of wireless propagation mechanisms. To get a complete picture of the end-to-end efficiency of a wireless power transfer system, we see that the interplay of its individual components may unveil challenges beyond a (sometimes theoretical) analysis of its individual building blocks. Circuit simulations and measurements shine light on these challenges: Recent literature indicates that *frequency diversity* (facilitating e.g. high-PAPR waveforms) may be exploited to benefit from the nonlinear behavior of EN device front-ends and increase their energy harvesting (EH) efficiency. By means of simulation and measurement, however, we were not able to confirm this gain with actual EH hardware, as demonstrated in Chapter 4. Combined with the losses incurring due to broadband matching and increased hardware complexity, our analysis indicates that the harvesting efficiency of an EN device may benefit from a single-tone waveform.

To enable more dedicated experiments and measurements, we designed a demonstrator of an

EH device presented in Chapter 5 and discuss the challenges that come along. We demonstrate a method of directly matching the EH circuit to the antenna and thereby omitting a lossy matching network, which results both in an efficient design and a small form factor.

In summary, the analyses presented in this deliverable prove many of the achievable gains promised in the REINDEER deliverable D4.1 [1], where we particularly highlighted the unprecedented efficiency attained with large arrays operating at sub-10 GHz. The synergies of environment-awareness (including positioning, mapping and geometry-based beamforming) and measurement-based beamforming will be more closely investigated in deliverable D4.3, constituting the concluding work of the REINDEER consortium in WP4.

# Appendix A

## MISO channel model

In [12], we introduced a geometry-based channel model for WPT with isotropic antennas. This initial model is based on an image source model [42], where SMCs originating from extended, flat surfaces, e.g., walls, are modeled by mirroring the antennas  $\ell$  of a transmitting RW across these surfaces. We model  $k \in \{1, \dots, K\}$  SMCs including the LoS, where each reflection is associated with a reflection coefficient  $\gamma_k$ . We extended the model in [1] to accommodate antennas with arbitrary gain patterns  $G(\theta, \varphi)$ , where  $\theta$  and  $\varphi$  are elevation and azimuth angles within the local coordinate system of each antenna  $\ell$ . Furthermore, possible polarization losses  $g_{k,\ell}^{\text{pol}}$  due to a polarization mismatch between transmit and receive antennas as well as polarization shifts due to reflections are accounted for. Our most complete channel model is defined in [8], where we model the visibility of an SMC through a visibility vector  $\chi_k$ . This becomes of particular significance with distributed RWs and physically large arrays where specific SMCs are only visible over a part of the antennas. To consider these effects, we define the radio channel  $\mathbf{h}$  as

$$\mathbf{h} = \sum_{k=1}^K \mathbf{h}_k(\mathbf{p}) + \mathbf{h}_{\text{DM}} \quad (\text{A.1})$$

consisting of  $K$  SMCs related to the environment geometry, and diffuse multipath denoted as  $\mathbf{h}_{\text{DM}}$ .

### Specular Multipath

Each SMC channel vector  $\mathbf{h}_k(\mathbf{p})$  is modeled as

$$\mathbf{h}_k(\mathbf{p}) = \mathbf{A}_k(\mathbf{p}) \mathbf{G}_k(\mathbf{p}) \mathbf{b}_k(\mathbf{p}) \quad (\text{A.2})$$

with the matrices  $\mathbf{A}_k(\mathbf{p}) = \text{diag}([\chi_{k,1}(\mathbf{p}) \dots \chi_{k,L}(\mathbf{p})])$  accounting for the SMC visibility<sup>1</sup> per array element, where

$$[\chi]_{\ell} = \begin{cases} 1, & \text{component visible} \\ 0, & \text{component not visible} \end{cases} \quad (\text{A.3})$$

<sup>1</sup>Please refer to the appendix of [10] for a description on how to compute the visibility vector  $\chi_k$ .

and  $\mathbf{G}_k(\mathbf{p}) = \text{diag}([g_{k,1}(\mathbf{p}), \dots, g_{k,L}(\mathbf{p})])$  containing the gain pattern values of each transmit antenna  $\ell$  and the receive antenna as well as the SISO path loss, i.e.,

$$g_{k,\ell}(\mathbf{p}) = \sqrt{G_{t,\ell}} \sqrt{G_r} \frac{\lambda}{4\pi d_{k,\ell}} \gamma^k g_{k,\ell}^{\text{pol}}, \quad (\text{A.4})$$

where the dependency on the look angles is omitted for notational brevity and  $d_{k,\ell}$  is the distance of each antenna  $\ell$  from each mirror source to the EN device.

The vector  $\mathbf{b}_k(\mathbf{p}) = [e^{-jk_0 d_{k,1}(\mathbf{p})} \dots e^{-jk_0 d_{k,L}(\mathbf{p})}]^T$  contains the phase shifts due to the distances  $d_{k,\ell}$  traveled from the RW to the EN device, with  $k_0 = \frac{2\pi}{\lambda}$  denoting the spatial angular frequency.

## Diffuse Multipath

The DM contained in  $\mathbf{h}_{\text{DM}}$  is used to represent an often large number of components that are either not resolvable due to the measurement aperture or cannot be related to the environment without involved modeling, e.g., ray-tracing. A number of statistical models are popular in the literature. In [43], surface roughness was used to model non-specular reflections, allowing a smooth transition from specular to diffuse reflection. In [44] an autoregressive process was used, whereas [45], [46] model the DM as the result of the convolution of the transmit signal with a random process. A geometry-related approach was taken in [8], [47], [48], where randomly distributed point source scatterers are used to model diffuse paths.

## Appendix B

# Reciprocity Property of Radio Channels

A two-port

$$\mathbf{S} = \begin{bmatrix} S_{11} & S_{12} \\ S_{21} & S_{22} \end{bmatrix} \quad (\text{B.1})$$

given through its respective S-parameters is called *reciprocal* if  $\mathbf{S}$  is symmetric [49, p. 181f.]. When acquiring radio channels between antennas, e.g., antenna 1 connected to port 1 of a VNA and antenna 2 connected to port 2, we usually measure the  $S_{21}(f)$  parameter. It defines the amplitude and phase of a power wave amplitude  $b_2 \in \mathbb{C}$  transmitted to port 2 given that a power wave amplitude  $a_1 \in \mathbb{C}$  is incident at port 1 and no power wave  $a_2$  is incident at port 2 (i.e., port 2 is perfectly matched) thus,

$$S_{21} = \left. \frac{b_2}{a_1} \right|_{a_2=0}. \quad (\text{B.2})$$

When a EN device transmits a pilot sequence from its antenna to a RW with  $L_t$  antennas, then the elements of a single-input multiple-output (SIMO) channel vector are estimated, i.e., estimates of  $S_{12}(f)_\ell \triangleq [\mathbf{h}(f)]_\ell$ , between a RW antenna  $\ell \in \{1 \dots L_t\}$  and the EN device antenna. Through the *reciprocity property*, i.e.,  $S_{12}(f)_\ell = S_{21}(f)_\ell$ , the same channel vector  $\mathbf{h}(f)$  is both the SIMO channel vector in the uplink and the MISO channel vector in the downlink. Thus, by computing downlink precoding weights  $\mathbf{w}$  on a channel estimate  $\hat{\mathbf{h}}$  acquired (e.g., measured) on the uplink, the reciprocity property is inherently exploited, hence the term *reciprocity-based* precoding.

It should be mentioned, however, that the RF chains within an EN device frontend are in general different in the transmitting and receiving modes, thus the *reciprocity* property is not given for this part of the channel. Related work on that subject investigates how to deal with these non-reciprocal transmit/receive chains [50].

## Appendix C

# Confidence associated with uncertainty intervals

To elaborate the confidence associated with the  $n\sigma$ -intervals depicted in Fig. 2.2, we compute the confidence levels

$$\zeta^{(n)}(\text{SNR}) = \frac{m_n(\text{SNR})}{M} \quad (\text{C.1})$$

as the ratio of realizations  $m_n$  within the interval to the number of realizations  $M$  generated in the MC analysis. We choose  $M = 10^6$  for this analysis and compute  $\zeta^{(n)}(\text{SNR})$  for  $n \in \{1, 2, 3\}$  versus the quality of CSI expressed through the channel SNR for both the amplitude  $|y|$  and the path gain  $PG$ . In more detail than elaborated in Section 2.1.2, the results in Fig. C.1 show that the confidence levels  $\zeta_{|y|}^{(n)}(\text{SNR})$  for the amplitude corresponds well with the respective confidence levels of a Rayleigh-distribution, while the confidences level  $\zeta_{PG}^{(n)}(\text{SNR})$  for the path gain corresponds with the respective confidence levels of a chi-squared distribution in the low SNR regime. Transitioning to the linear regime, both the distribution for the amplitude  $|y|$  and the distribution for the path gain  $PG$  approach a normal distribution. The confidence levels  $\zeta_{|y|}^{(n)}(\text{SNR})$  and  $\zeta_{PG}^{(n)}(\text{SNR})$  for a random realization of an amplitude  $|y|$  and respective path gain  $PG$  to be located in within the  $n\sigma$ -intervals consequently match with the corresponding confidence levels of a normal distribution.

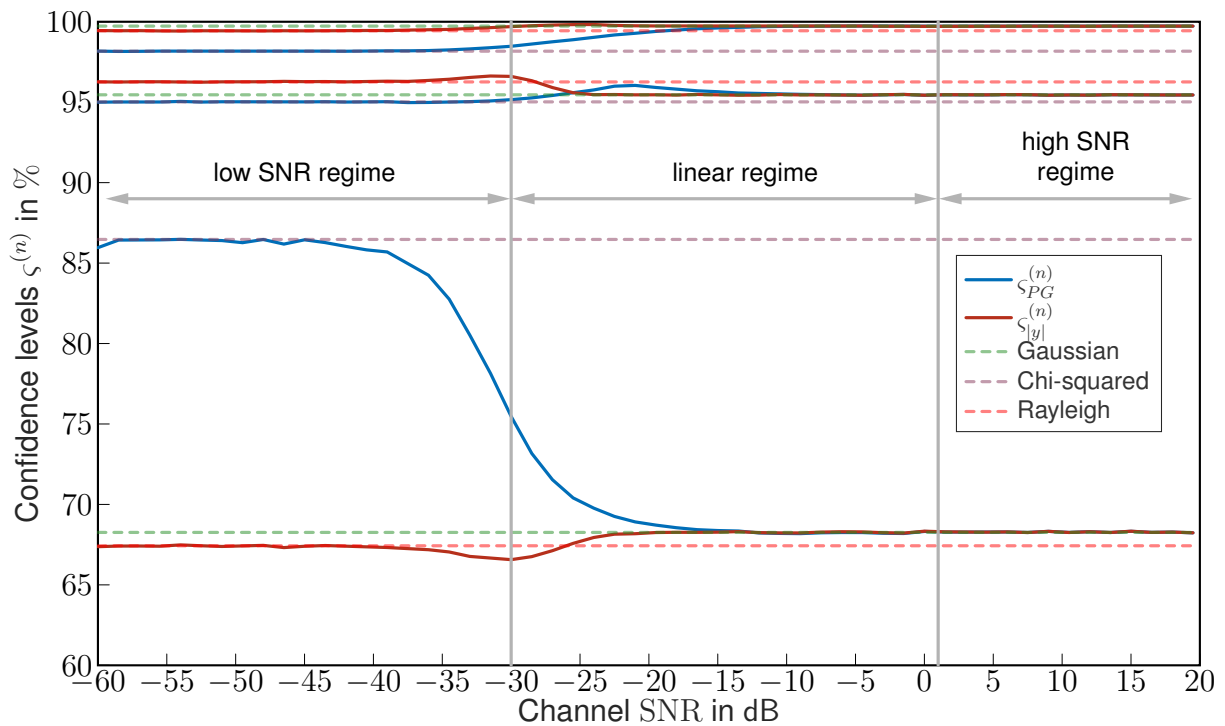


Figure C.1: Confidence levels  $\zeta^{(n)}(\text{SNR})$  that a random realization of an amplitude  $|y|$  or path gain  $PG$  is located within the interval  $PG_R \pm n\sigma$  with  $PG_R$  from (2.14) versus the channel SNR defined in (2.12). The confidence levels have been computed by evaluating C.1 on a MC analysis with  $M = 10^6$  realizations. The three lines corresponding to a single linestyle correspond to the variations of  $n = \{1, 2, 3\}$ . The confidence levels correspond to the intervals depicted in Fig. 2.2.

## Bibliography

- [1] C. Buyle, B. Cox, D. Delabie, B. Deutschmann, T. Wilding, M. Graber, K. Witrissal, and U. Mühlmann, "System design study for energy-neutral devices interacting with the RadioWeaves infrastructure," REINDEER project, Deliverable ICT-52-2020 / D4.1, Oct. 2022.
- [2] REINDEER project, "Assessment of signalling schemes, protocols, and algorithms for energy-neutral devices," Deliverable ICT-52-2020 / D4.3, unpublished (2024).
- [3] O. Edfors, R. Brazil, H. Petautschnig, G. Callebaut, T. Feys, L. V. der Perre, E. G. Larsson, O. Edfors, E. Fitzgerald, L. Liu, J. R. Sanchez, W. Tärneberg, P. Frenger, B. Deutschmann, T. Wilding, and K. Witrissal, "RadioWeaves high-level architecture and processing distribution strategies," REINDEER project, Deliverable ICT-52-2020 / D2.1, Jan. 2022. DOI: 10.5281/zenodo.5938909. [Online]. Available: <https://doi.org/10.5281/zenodo.5938909>.
- [4] REINDEER project, "Position estimation and environment learning," Deliverable ICT-52-2020 / D3.3, unpublished (2023).
- [5] REINDEER project, "Hardware requirements to support energy transfer to energy-neutral nodes," Deliverable ICT-52-2020 / D2.3, unpublished (2023).
- [6] C. Peel, B. Hochwald, and A. Swindlehurst, "A vector-perturbation technique for near-capacity multi-antenna multiuser communication-part I: channel inversion and regularization," *IEEE Transactions on Communications*, vol. 53, no. 1, pp. 195–202, 2005. DOI: 10.1109/TCOMM.2004.840638.
- [7] T. L. Marzetta, E. G. Larsson, H. Yang, and H. Q. Ngo, *Fundamentals of Massive MIMO*. Cambridge, UK: Cambridge University Press, 2016.
- [8] REINDEER Project, "Propagation characteristics and channel models for RadioWeaves including reflector-rays," Deliverable ICT-52-2020 / D1.2, 2023 (unpublished).
- [9] P. Viswanath, D. Tse, and R. Laroia, "Opportunistic beamforming using dumb antennas," *IEEE Transactions on Information Theory*, vol. 48, no. 6, pp. 1277–1294, 2002. DOI: 10.1109/TIT.2002.1003822.
- [10] B. J. B. Deutschmann, T. Wilding, M. Graber, and K. Witrissal, "XL-MIMO channel modeling and prediction for wireless power transfer," in *WS10 IEEE ICC 2023 Workshop on Near-Field Localization and Communication for 6G*, Rome, Italy, May 2023.
- [11] D. Johnson and D. Dudgeon, *Array Signal Processing: Concepts and Techniques* (Prentice-Hall Series in Signal). Prentice Hall, 1993, ISBN: 9780130485137.
- [12] B. J. B. Deutschmann, T. Wilding, E. G. Larsson, and K. Witrissal, "Location-based Initial Access for Wireless Power Transfer with Physically Large Arrays," in *WS08 IEEE ICC 2022 Workshop on Synergies of communication, localization, and sensing towards 6G (WS08 ICC'22 Workshop - ComLS-6G)*, Seoul, Korea (South), May 2022.
- [13] D. Mishra and E. G. Larsson, "Optimal Channel Estimation for Reciprocity-Based Backscattering with a Full-Duplex MIMO Reader," *IEEE Transactions on Signal Processing*, vol. 67, no. 6, pp. 1662–1677, 2019.
- [14] J. R. Costa, C. R. Medeiros, and C. A. Fernandes, "Performance of a Crossed Exponentially Tapered Slot Antenna for UWB Systems," *IEEE Transactions on Antennas and Propagation*, vol. 57, no. 5, pp. 1345–1352, May 2009, ISSN: 0018-926X. DOI: 10.1109/TAP.2009.2016727.
- [15] Joint Committee for Guides in Metrology (JCGM), "Guide to the Expression of Uncertainty in Measurement (GUM): Evaluation of Measurement Data," 2008.
- [16] C. A. Balanis, *Antenna Theory: Analysis and Design*, 3rd ed. Hoboken, NJ: John Wiley & Sons, 2005, p. 1136, ISBN: 9780471667827.
- [17] M.-K. Olkkonen, V. Mikhnev, and E. Huuskonen-Snicker, "Complex permittivity of concrete in the frequency range 0.8 to 12 GHz," in *2013 7th European Conference on Antennas and Propagation (EuCAP)*, 2013, pp. 3319–3321.
- [18] G. Callebaut, J. Van Mulders, G. Ottoy, D. Delabie, B. Cox, N. Stevens, and L. Van der Perre, "Textile–open 6G R&D testbed for communication, positioning, sensing, WPT and federated learning," in *2022 Joint*

- European Conference on Networks and Communications & 6G Summit (EuCNC/6G Summit)*, IEEE, 2022, pp. 417–422.
- [19] G. Callebaut, J. Van Mulders, G. Ottoy, and L. Van der Perre, “A primer on techtile: An R&D testbed for distributed communication, sensing and positioning,” *arXiv preprint arXiv:2105.06740*, 2021.
- [20] A. Blanco, N. Ludant, P. J. Mateo, Z. Shi, Y. Wang, and J. Widmer, “Performance Evaluation of Single Base Station ToA-AoA Localization in an LTE Testbed,” in *2019 IEEE 30th Annual International Symposium on Personal, Indoor and Mobile Radio Communications (PIMRC)*, 2019, pp. 1–6. DOI: 10.1109/PIMRC.2019.8904454.
- [21] M. Henninger, S. Mandelli, M. Arnold, and S. T. Brink, “A Computationally Efficient 2D MUSIC Approach for 5G and 6G Sensing Networks,” in *2022 IEEE Wireless Communications and Networking Conference (WCNC)*, IEEE, Apr. 2022. DOI: 10.1109/wcnc51071.2022.9771837.
- [22] R. Schmidt, “Multiple emitter location and signal parameter estimation,” *IEEE Transactions on Antennas and Propagation*, vol. 34, no. 3, pp. 276–280, 1986. DOI: 10.1109/TAP.1986.1143830.
- [23] Q. Yan, J. Chen, G. Ottoy, and L. De Strycker, “Robust AOA based acoustic source localization method with unreliable measurements,” *Signal Processing*, vol. 152, pp. 13–21, 2018, ISSN: 0165-1684. DOI: <https://doi.org/10.1016/j.sigpro.2018.05.010>. [Online]. Available: <https://www.sciencedirect.com/science/article/pii/S0165168418301701>.
- [24] M. F. Özkoç, C. Tunc, and S. S. Panwar, “Data-Driven Beamforming Codebook Design to Improve Coverage in Millimeter Wave Networks,” in *2022 IEEE 95th Vehicular Technology Conference: (VTC2022-Spring)*, 2022, pp. 1–7. DOI: 10.1109/VTC2022-Spring54318.2022.9860648.
- [25] A. B. Gershman, N. D. Sidiropoulos, S. Shahbazpanahi, M. Bengtsson, and B. Ottersten, “Convex Optimization-Based Beamforming,” *IEEE Signal Processing Magazine*, vol. 27, no. 3, pp. 62–75, 2010. DOI: 10.1109/MSP.2010.936015.
- [26] S. Basharat, S. A. Hassan, A. Mahmood, Z. Ding, and M. Gidlund, “Reconfigurable intelligent surface-assisted backscatter communication: A new frontier for enabling 6G IoT networks,” *arXiv preprint arXiv:2107.07813*, 2021.
- [27] J. Kimionis, A. Bletsas, and J. N. Sahalos, “Increased range bistatic scatter radio,” *IEEE Trans. Commun.*, vol. 62, no. 3, pp. 1091–1104, Mar. 2014.
- [28] R. Biswas, M. U. Sheikh, H. Yiğitler, J. Lempiäinen, and R. Jäntti, “Direct path interference suppression requirements for bistatic backscatter communication system,” in *Proc. IEEE 93rd Veh. Technol. Conf. (VTC-Spring)*, Apr. 2021.
- [29] C. Mollen, J. Choi, E. G. Larsson, and R. W. Heath, “Uplink performance of wideband massive MIMO with one-bit ADCs,” *IEEE Trans. Wireless Commun.*, vol. 16, no. 1, pp. 87–100, Oct. 2016.
- [30] A. Varshney, O. Harms, C. Pérez-Penichet, C. Rohner, F. Hermans, and T. Voigt, “Lorea: A backscatter architecture that achieves a long communication range,” in *Proc. ACM Conf. Embedded Netw. Sensor Syst.*, Nov. 2017.
- [31] D. Li, “Capacity of backscatter communication with frequency shift in Rician fading channels,” *IEEE Wireless Commun. Lett.*, vol. 8, no. 6, pp. 1639–1643, Dec. 2019.
- [32] Q. Tao, Y. Li, C. Zhong, S. Shao, and Z. Zhang, “A novel interference cancellation scheme for bistatic backscatter communication systems,” *IEEE Commun. Lett.*, vol. 25, no. 6, pp. 2014–2018, Jun. 2021.
- [33] Z. B. Zawawi, Y. Huang, and B. Clerckx, “Multiuser wirelessly powered backscatter communications: Nonlinearity, waveform design, and SINR-energy tradeoff,” *IEEE Trans. Wireless Commun.*, vol. 18, no. 1, pp. 241–253, Nov. 2018.
- [34] M. Hua, L. Yang, C. Li, Z. Zhu, and I. Lee, “Bistatic backscatter communication: Shunt network design,” *IEEE Internet Things J.*, vol. 8, no. 9, pp. 7691–7705, Nov. 2020.
- [35] H. Guo, Q. Zhang, S. Xiao, and Y.-C. Liang, “Exploiting multiple antennas for cognitive ambient backscatter communication,” *IEEE Internet Things J.*, vol. 6, no. 1, pp. 765–775, Jul. 2018.
- [36] D. Dobkin, *The RF in RFID*, 2nd ed. New York, NY, USA: Newnes, 2013.
- [37] A. Boaventura, A. Collado, N. B. Carvalho, and A. Georgiadis, “Optimum behavior: Wireless power transmission system design through behavioral models and efficient synthesis techniques,” *IEEE Microwave Magazine*, vol. 14, no. 2, pp. 26–35, 2013.
- [38] B. Clerckx and E. Bayguzina, “Low-complexity adaptive multisine waveform design for wireless power transfer,” *IEEE Antennas and Wireless Propagation Letters*, vol. 16, pp. 2207–2210, 2017.
- [39] N. Shariati, J. R. Scott, D. Schreurs, and K. Ghorbani, “Multitone excitation analysis in RF energy harvesters—considerations and limitations,” *IEEE Internet of Things Journal*, vol. 5, no. 4, pp. 2804–2816, 2018.
- [40] F. Bolos, J. Blanco, A. Collado, and A. Georgiadis, “RF energy harvesting from multi-tone and digitally modulated signals,” *IEEE Transactions on Microwave Theory and Techniques*, vol. 64, no. 6, pp. 1918–1927, 2016. DOI: 10.1109/TMTT.2016.2561923.

- [41] *Evaluation board for AEM40940*, AEM40940, Rev. 1.0, e-Peas semiconductors, Jan. 2018.
- [42] E. Leitinger, P. Meissner, C. Rudisser, G. Dumphart, and K. Witrissal, "Evaluation of Position-Related Information in Multipath Components for Indoor Positioning," vol. 33, no. 11, pp. 2313–2328, Nov. 2015, ISSN: 0733-8716. DOI: [10.1109/JSAC.2015.2430520](https://doi.org/10.1109/JSAC.2015.2430520).
- [43] J. Kulmer, F. Wen, N. Garcia, H. Wymeersch, and K. Witrissal, "Impact of Rough Surface Scattering on Stochastic Multipath Component Models," in *2018 IEEE 29th Annual International Symposium on Personal, Indoor and Mobile Radio Communications (PIMRC)*, 2018, pp. 1410–1416. DOI: [10.1109/PIMRC.2018.8580964](https://doi.org/10.1109/PIMRC.2018.8580964).
- [44] J. Salmi, J. Poutanen, K. Haneda, A. Richter, V.-M. Kolmonen, P. Vainikainen, and A. Molisch, "Incorporating diffuse scattering in geometry-based stochastic MIMO channel models," in *Proceedings of the Fourth European Conference on Antennas and Propagation*, IEEE, 2010, pp. 1–5.
- [45] A. Richter, "Estimation of Radio Channel Parameters: Models and Algorithms," Ph.D. dissertation, Ilmenau University of Technology, 2005.
- [46] K. Witrissal and P. Meissner, "Performance bounds for multipath-assisted indoor navigation and tracking (MINT)," in *2012 IEEE International Conference on Communications (ICC)*, 2012, pp. 4321–4325. DOI: [10.1109/ICC.2012.6363827](https://doi.org/10.1109/ICC.2012.6363827).
- [47] J. Flordelis, X. Li, O. Edfors, and F. Tufvesson, "Massive MIMO Extensions to the COST 2100 Channel Model: Modeling and Validation," vol. 19, no. 1, pp. 380–394, 2020. DOI: [10.1109/TWC.2019.2945531](https://doi.org/10.1109/TWC.2019.2945531).
- [48] F. M. Schubert, M. L. Jakobsen, and B. H. Fleury, "Non-stationary propagation model for scattering volumes with an application to the rural LMS channel," vol. 61, no. 5, pp. 2817–2828, 2013.
- [49] D. M. Pozar, *Microwave Engineering*, 4th ed. Hoboken, NJ: John Wiley & Sons, 2011, p. 732, ISBN: 9781118213636.
- [50] J. Vieira, F. Rusek, and F. Tufvesson, "Reciprocity calibration methods for massive mimo based on antenna coupling," in *2014 IEEE Global Communications Conference*, 2014, pp. 3708–3712. DOI: [10.1109/GLOCOM.2014.7037384](https://doi.org/10.1109/GLOCOM.2014.7037384).